

Kinematics of Circumgalactic O VI Gas and Disk Rotation of $z \approx 0.2$ Star-forming Galaxies

STEPHANIE H. HO,¹ CRYSTAL L. MARTIN,² HASTI NATEGHI,³ GLENN G. KACPRZAK,³ AND JONATHAN STERN⁴

¹Department of Astronomy, New Mexico State University, Las Cruces, NM 88003, USA

²Department of Physics, University of California, Santa Barbara, CA 93106, USA

³Centre for Astrophysics and Supercomputing, Swinburne University of Technology, Hawthorn, VIC 3122, Australia

⁴School of Physics and Astronomy, Tel Aviv University, Tel Aviv 69978, Israel

ABSTRACT

Quasar sightline observations reveal that low-ionization-state gas corotates with the galaxy disk and often at sub-centrifugal velocities, suggesting that the gas is spiraling towards the galaxy disk. However, while observations ubiquitously detect O VI absorption around low-redshift, $\sim L^*$ star-forming galaxies, the relationship between O VI and the galaxy disk, especially the kinematics, is not well-established. This work focuses on the O VI kinematics and its comparison with that of the low ions and galactic disk rotation. We present observations of 18 pairs of quasars and $z \approx 0.2$ star-forming galaxies. All quasar sightlines intersect the circumgalactic medium (CGM) within 45° from the galaxy major axes. We show that while individual O VI velocity components do not correlate with disk rotation, the bulk of O VI gas in individual sightlines rarely counter-rotates. We then match O VI velocity components with those of low ions by minimizing the difference of their velocity centroids. The O VI velocity components with successful low-ion matches are typically found at small sightline impact parameters and are more likely to corotate with the disk. We suggest that the low-ion-matched O VI velocity components trace the gas co-spatial with the low ions near the extended disk plane in the inner CGM, whereas those without low-ion matches represent the gas at large 3D radii. While the gas at large radii is theoretically expected to kinematically correlate with the disk angular momentum, this correlation is expected to be weaker due to the higher turbulent to mean rotation velocity ratio at large radii, consistent with our results.

Keywords: Circumgalactic medium (1879), Extragalactic astronomy (506), Quasar absorption line spectroscopy (1317)

1. INTRODUCTION

The interplay between galaxies and their surrounding gas shapes the evolution of galaxies. Galaxies gather gas from their surroundings to form stars, whereas winds driven by supernovae and active galactic nuclei (AGN) remove gas from the galaxies and slow star formation. The surrounding gas, known as the circumgalactic medium (CGM), is a substantial reservoir of baryons and metals and extends at least to the virial radius (r_{vir}) of galaxies (see Tumlinson et al. 2017 and Faucher-Giguère & Oh 2023 for reviews). Because the low gas density makes direct imaging of the CGM challenging, quasar spectroscopy serves as a powerful tool

for detecting the CGM in absorption and characterizing CGM properties.

The ubiquitous detection of O VI $\lambda\lambda 1031, 1037$ absorption around low-redshift, $\sim L^*$ star-forming galaxies in contrast to the low detection rate around quiescent galaxies have received significant attention (Tumlinson et al. 2011; Tchernyshov et al. 2023). Dwarf galaxies also show the same contrast (Dutta et al. 2024), even though the O VI detection rate and column density of star-forming dwarf galaxies are lower than that of $\sim L^*$ galaxies (Johnson et al. 2015, 2017; Tchernyshov et al. 2022; Mishra et al. 2024). The origin of this “O VI dichotomy” remains controversial. AGN feedback possibly leads to a low CGM mass fraction, resulting in the low O VI detection rate of quiescent galaxies (Suresh et al. 2017; Nelson et al. 2018; Davies et al. 2020). Some work argued that the quiescent galaxies have higher average halo masses than the star-forming galaxies in the ob-

Corresponding author: Stephanie Ho
 shho@nmsu.edu

served galaxy samples, and hence, the higher virial temperatures promote oxygen to higher ionization states. In particular, the predicted CGM properties change significantly for galaxies with halo masses around $\sim 10^{12} M_{\odot}$ due to virialization (Oppenheimer et al. 2016; Mathews & Prochaska 2017; Stern et al. 2018; Sultan et al. 2025). However, recent work with a mass-controlled galaxy sample still found the “O VI dichotomy”. This implies a potential connection between O VI and ongoing star formation, for which the transformation of CGM happens concurrently with the quenching of galaxies (Tchernyshyov et al. 2023).

Dedicated efforts with quasar absorption-line studies have analyzed the circumgalactic O VI properties of star-forming galaxies and compared that with the cool gas ($\sim 10^4$ K) traced by low-ionization-state ions (e.g., Mg II). For $\sim L^*$ star-forming galaxies, the cool gas is typically detected only in the inner CGM of ~ 100 kpc, and the strength of the low-ionization-state absorption decreases sharply with increasing projected separation from the galaxies (Chen et al. 2010; Nielsen et al. 2013; Huang et al. 2021). In contrast, O VI is detected in sightlines out to at least two to three times the galaxy virial radius, and the O VI column density only declines slowly with the sightline impact parameters (Tumlinson et al. 2011; Tchernyshyov et al. 2022; Qu et al. 2024). Similarly for star-forming dwarf galaxies, O VI has a higher detection rate and a more extended distribution compared to that of the low ions (Mishra et al. 2024; Dutta et al. 2024). But surprisingly, both low ions and O VI exhibit a bimodal distribution with azimuthal angle¹ (Bouché et al. 2012; Kacprzak et al. 2012, 2015; Schroetter et al. 2019). The bimodality in gas distribution is also supported by recent cloud-by-cloud multi-phase, ionization modelings that indicate a larger number of clouds in sightlines near the galaxy major and minor axes (Sameer et al. 2024).

In addition to the spatial distribution, kinematics provides crucial information for understanding the origin and properties of the CGM traced by O VI and low-ionization-state ions. While O VI absorption has a larger velocity spread compared to that of the low ions, they typically span similar velocity ranges (Werk et al. 2016; Nielsen et al. 2017). However, while the absorption of low ions becomes broader and stronger towards the galaxy minor axes, a result attributed to gas kinematically disturbed by outflows (Bordoloi et al. 2011; Martin et al. 2019; Schroetter et al. 2019), the O VI veloc-

ity spread does not vary with the sightline azimuthal angle and galaxy disk inclination (Nielsen et al. 2017). Furthermore, for sightlines near the galaxy major axes, the cool gas (traced by Mg II) corotates with the galaxy disk and often at sub-centrifugal velocities (Steidel et al. 2002; Kacprzak et al. 2010, 2011; Ho et al. 2017; Zabl et al. 2019), suggesting that the gas is infalling (Ho & Martin 2020). On the other hand, the lack of correlation between O VI kinematics and disk rotation potentially implies that O VI alone does not serve as a useful tracer for galaxy gas accretion (Kacprzak et al. 2019, 2025).

On the one hand, with the spatially extended distribution of O VI compared to low ions, it is perhaps unsurprising that the O VI kinematics do not seem to correlate with disk rotation as the low-ionization-state counterparts. In particular, because the CGM angular momentum remains roughly constant with radius, the outer CGM is expected to have a lower mean rotation velocity, resulting in a weaker correlation with the disk rotation. But on the other hand, in contrast to the large number of literatures that observationally confirmed the corotation between Mg II gas and the galaxy disk, only very few work has performed this kinematics comparison with O VI (Kacprzak et al. 2019; Nateghi et al. 2024; Kacprzak et al. 2025).

In this paper, we build a sample of star-forming galaxies with quasar sightlines near the galaxy major axes and exclude galaxies with face-on disks. With quasar spectroscopy from the *Cosmic Origin Spectrograph (COS)* on the *Hubble Space Telescope (HST)* and galaxy rotation curve measurements, we analyze and compare the kinematics of the CGM traced by O VI and low ions (e.g., Si II, Si III) with the galaxy disk rotation. We describe the sample selection, data reduction, and measurements in Section 2. In Section 3, we present the results of the kinematics comparison among O VI gas, low-ionization-state gas, and disk rotation. We interpret our results and discuss their implications in Section 4. Finally, Section 5 summarizes the conclusions. Throughout the paper, we adopt the cosmology from Planck Collaboration et al. (2016), with $h = 0.6774$, $\Omega_m = 0.3089$, $\Omega_{\Lambda} = 0.6911$, and $\Omega_b = 0.0486$.

2. DATA AND OBSERVATIONS

We present the analyses of 18 galaxy-quasar pairs to study the kinematics of O VI and low-ionization-state absorbers and their relationship with galaxy disk rotation. We conducted quasar spectroscopy with *HST/COS*, including new spectra from our *HST* program and archival observations. We also acquired galaxy spectra from multiple ground-based telescopes. We describe our sample selection in Section 2.1. Sec-

¹ The azimuthal angle α is defined as the angle between the galaxy major axis and the line drawn between the center of the galaxy and the quasar.

tion 2.2 discusses the galaxy spectroscopic observations and rotation curve measurements, and Section 2.3 describes the galaxy properties. In Section 2.4, we describe the *HST/COS* observations and measurements of absorption-line systems.

2.1. Sample of Galaxy–Quasar Pairs

Our study focuses star-forming galaxies with quasar sightlines near the major axes of the galaxies. The galaxy–quasar pairs were selected from published literature with known galaxy disk orientation; the disk geometry was obtained either from published work or from the Sloan Digital Sky Survey (SDSS; Blanton et al. 2017). We restricted our sample to galaxies with inclined disks of inclination angles of $i \gtrsim 45^\circ$, and each sightline lies within 45° from the galaxy major axis, i.e., with azimuthal angle $\alpha \leq 45^\circ$.

The compiled sample consists of 18 galaxy–quasar pairs with a median galaxy redshift of $z \approx 0.21$. Tables 1 and 2 specify the coordinates and properties of galaxies, respectively, and Table 3 lists the coordinates of the paired quasars. Figure 1 shows the location of the quasar sightlines relative to the projected major and minor axes of the galaxies on the sky. The impact parameter d of the quasar sightlines span between 20 and 284 kpc. The majority of the sightlines intersect the galaxies within 100 kpc, which corresponds to less than half of the virial radius (r_{vir}) as indicated by the colors of the markers (see Section 2.3).

2.2. Galaxy Spectroscopy

We used the galaxy spectra to measure the systemic redshifts of the target galaxies and their rotation curves from the optical emission lines. We acquired new long-slit galaxy spectra with the Blue and Red Channel Spectrographs at the MMT Observatory. We also compiled previous observations (Ho et al. 2017; Martin et al. 2019; Kacprzak et al. 2019) from the Low Resolution Imaging Spectrometer (LRIS; Oke et al. 1995; Rockosi et al. 2010) and the Echellette Spectrograph and Imager (ESI; Sheinis et al. 2002) at the W. M. Keck Observatory and the Double Imaging Spectrograph (DIS) at the Apache Point Observatory (APO) 3.5 m telescope.²

We summarize the galaxy observations in Table 1. Section 2.2.1 describes the new MMT observations, and Sections 2.2.2 and 2.2.3 briefly discuss the previous Keck and APO observations, respectively. Section 2.2.4 de-

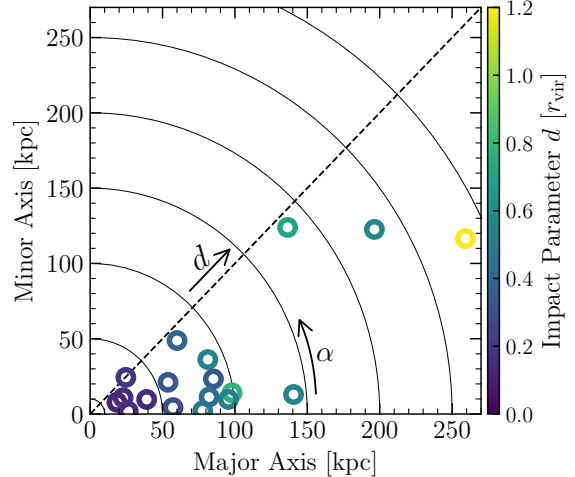


Figure 1. Ensemble of 18 sightlines. All selected galaxies have inclined disks with inclination angles $i \gtrsim 45^\circ$. Each sightline intersects the galaxy near the major axis with azimuthal angle $\alpha \leq 45^\circ$. The impact parameter d of the quasar sightlines ranges between 20 and 284 kpc. The color of the markers represents the sightline impact parameter normalized by the galaxy virial radius. Most sightlines intersect the inner CGM within 100 kpc (i.e., within $0.5r_{\text{vir}}$).

scribes the measurements of the galaxy rotation curves from the emission lines (typically H α) detected in the galaxy spectra.

2.2.1. MMT Blue and Red Channel Observations

We conducted new galaxy spectroscopic observations using the MMT Blue and Red Channel Spectrographs. On February 28, 2020, we observed the galaxies with the Blue Channel and configured it with the 832 lines mm $^{-1}$ grating blazed at 7790 Å. On January 9, 2021, we used the Red Channel with the 1200 lines mm $^{-1}$ grating blazed at 7700 Å. For both observations, we applied the blue blocking filter R-63 to block the higher order light. We used the default 1 × 1 detector binning, which provided a pixel scale of 0''.3 for both channels and a wavelength dispersion of 0.72 Å pixel $^{-1}$ and 0.80 Å pixel $^{-1}$ for the Blue and Red Channel, respectively. We observed the target galaxies by aligning the 1''.0-wide long-slit with the galaxy major axes. For both channels, the 1''.0-wide slitlet provided a spectral resolution of 75–85 km s $^{-1}$ full width at half maximum intensity (FWHM).

The data were reduced using IRAF (Tody 1986, 1993) following standard procedures. For individual exposures, the zero-point bias level was corrected for, and the fixed pattern noise was removed using exposures of the internal quartz lamp. Cosmic rays were removed using L.A. Cosmic (van Dokkum 2001). Then, the frames

² Instrument specifications can be found in the manual written by Robert Lupton, which is available at http://www.apo.nmsu.edu/35m_operations/35m_manual/Instruments/DIS/DIS_usage.html#Lupton_Manual

Table 1. Galaxy Spectroscopy

Galaxy	Galaxy RA (J2000)	Galaxy DEC (J2000)	Instrument	Observing Date	Exposure Time (s)	Reference
J040150–054047	04:01:50.48	−05:40:47.07	MMT/Red Channel	2021 Jan 9	1800	This work
J080702+360141	08:07:02.27	+36:01:41.15	MMT/Blue Channel	2020 Feb 28	2700	This work
J084356+261855	08:43:56.12	+26:18:55.28	MMT/Blue Channel	2020 Feb 28	1800	This work
J085215+171137	08:52:15.36	+17:11:37.07	Keck/LRIS	2014 May 2	2640	Ho et al. (2017)
J091954+291345	09:19:54.11	+29:13:45.34	Keck/LRIS	2015 Mar 22	1760	Ho et al. (2017)
J094330+053118	09:43:30.67	+05:31:18.11	Keck/ESI	2016 Jan 15	4500	Kacprzak et al. (2019) [†]
J103643+565119	10:36:43.44	+56:51:19.00	Keck/LRIS	2015 Mar 22	1760	Ho et al. (2017)
J104117+061018	10:41:17.80	+06:10:18.88	Keck/ESI	2014 Apr 25	3300	Kacprzak et al. (2019) [†]
J113911–135108	11:39:11.52	−13:51:08.69	Keck/ESI	2016 Jan 15	1650	Kacprzak et al. (2019) [†]
J113909–135053	11:39:09.80	−13:50:53.08	Keck/ESI	2016 Jun 6	1800	Kacprzak et al. (2019) [†]
J123338+475757	12:33:38.87	+47:57:57.62	MMT/Red Channel	2021 Jan 9	2400	This work
J132222+464546	13:22:22.46	+46:45:46.18	Keck/ESI	2016 Jun 6	1500	Kacprzak et al. (2019) [†]
J135521+303320	13:55:21.20	+30:33:20.41	Keck/LRIS	2014 May 3	3520	Ho et al. (2017)
J142459+382113	14:24:59.82	+38:21:13.37	APO/DIS	2016 Apr 2	5100	Ho et al. (2017)
J154741+343350	15:47:41.46	+34:33:50.86	Keck/LRIS	2014 May 3	1760	Ho et al. (2017)
J155505+362848	15:55:05.27	+36:28:48.40	APO/DIS	2016 Jul 4	3200	Martin et al. (2019)
J160951+353838	16:09:51.62	+35:38:38.58	Keck/LRIS	2014 May 2	1760	Ho et al. (2017)
J225400+160925	22:54:00.58	+16:09:25.83	Keck/ESI	2016 Jun 6	1200	Kacprzak et al. (2019) [†]

[†]The ESI data were re-analyzed for galaxy rotation curve measurements.

were combined using a sigma-clipping algorithm to remove any remaining cosmic rays. A two-dimensional variance spectrum was computed when the exposures were combined. Frames of arc lamp exposures were used to calibrate the wavelength of the spectra, and the root-mean-square (rms) error of the dispersion solution was less than 15 km s^{-1} . The wavelength solution was checked using the calibrated night-sky emission-line spectrum from the Ultraviolet and Visual Echelle Spectrograph (Hanuschik 2003). Zero-point corrections were applied when necessary, which was caused by the difference in rotator angles between the science exposures and the calibration frames. This was followed by a heliocentric correction to correct for the earth’s seasonal motion.

From the two-dimensional galaxy spectra, we measured the galaxy rotation curves from the emission lines (Section 2.2.4). We also extracted an one-dimensional spectrum for each galaxy and determined the galaxy systemic redshift from the redshifted wavelengths of the H α , [N II] $\lambda\lambda 6548, 6583$, and [S II] $\lambda\lambda 6716, 6731$ emission lines.

2.2.2. Keck Observations

The Keck/LRIS observations were described in detail in Ho et al. (2017) and Martin et al. (2019). The LRIS double spectrograph was configured using the D500 dichroic, 1200 lines mm^{-1} grism blazed at 3400\AA

(LRISb) and the 900 lines mm^{-1} grism blazed at 5500\AA (LRISr). The galaxy emission lines for rotation curve measurements were captured by LRISr. The detectors were binned by two in both spatial and dispersion directions, which produced a spatial scale of $0''.27$ and a dispersion of $1.06 \text{ \AA pixel}^{-1}$. The $1''.0$ -wide long-slit was either aligned with the position angle of the major axis of the target galaxies, or masks of $1''.0$ -wide slitlets were designed to include nearby galaxies in the field. The $1''.0$ -wide slitlets provided an average resolution of $75\text{--}105 \text{ km s}^{-1}$ FWHM. The data reduction procedures for the LRISr spectra were explained in Ho et al. (2017) and were similar to those for reducing the MMT spectra described in Section 2.2.1.

The Keck/ESI observations were described in detail in Kacprzak et al. (2019). In brief, the galaxies were observed using the $1''.0$ -wide, $20''$ -long ESI slit, and the slitlet was aligned with the major axes of individual galaxies. The detector was binned by two in both the spatial and spectral directions. This produced a dispersion of $22 \text{ km s}^{-1} \text{ pixel}^{-1}$ and pixel scales of $0''.27$ to $0''.34$ over the echelle orders that covered the galaxy optical emission lines. The resulting spectral resolution from the $1''.0$ -wide slitlet was 90 km s^{-1} FWHM. Following the data reduction procedures as outlined in Kacprzak et al. (2019), we re-reduced the ESI spectra and re-examined the galaxy emission lines. The new

two-dimensional spectra were adopted to measure the galaxy rotation curves (Section 2.2.4).

2.2.3. APO DIS Observations

For galaxies J142459+38211 and J155505+362848, Ho et al. (2017) and Martin et al. (2019) conducted long-slit spectroscopy with APO/DIS to measure the galaxy rotation curves from the H α emission line. The 1''.5-wide long-slit was aligned with the major axis of each galaxy. The blue and red channels of DIS were configured with the 1200 lines mm $^{-1}$ blazed at 4400Å and 7300Å, respectively. The H α emission was detected by the red spectra, which had a spatial scale and dispersion of 0''.40 and 0.58 Å pixel $^{-1}$, respectively. The DIS spectra were reduced as discussed in Ho et al. (2017) and followed the same procedures as we reduced the MMT spectra. The spectral resolution was measured using the arclamps' lines as 50 km s $^{-1}$ FWHM.

2.2.4. Galaxy Rotation Curves

We generate the galaxy position–velocity (PV) maps by fitting a Gaussian profile to the galaxy emission lines at different spatial locations on the two-dimensional galaxy spectra. Following Ho et al. (2017), we convert the PV maps to rotation curve measurements by deprojecting the position and velocity measured along the slit onto circular orbits on the disk plane. For a slitlet at an angle ζ from the galaxy major axis, we calculate the galactocentric radius R from the projected distance ρ along the slit using

$$R = \rho \sqrt{1 + \sin^2 \zeta \tan^2 i}, \quad (1)$$

where i represents the disk inclination angle. We convert the line-of-sight velocity $v_{\text{los}}(\rho)$ to rotation velocity $V_{\text{rot}}(R)$ on the disk by

$$V_{\text{rot}}(R) = \frac{\sqrt{1 + \sin^2 \zeta \tan^2 i}}{\sin i \cos \zeta} v_{\text{los}}(\rho). \quad (2)$$

In the middle column of Figure 2, we show the line-of-sight velocity v_{los} and the rotation velocity V_{rot} of individual galaxies, which are represented by the cyan solid squares and black open circles, respectively.

To model the intrinsic rotation curves of the galaxies, we define a grid of rotation curves over a range of asymptotic rotation velocities V_∞ and turnover radii R_{RC} using an arctangent model,

$$V_{\text{model}}(R) = \frac{2}{\pi} V_\infty \arctan \frac{R}{R_{\text{RC}}}. \quad (3)$$

For each galaxy, we project the models onto the slit, convolve these projected models with a Gaussian model

for the seeing disk, and compare them to the PV maps measured from the galaxy emission lines. We minimize the fit residual to estimate V_∞ and R_{RC} for individual galaxies. In the middle column of Figure 2, the seeing-convolved model for each galaxy before and after the projection are shown using the black dashed and cyan solid curves, respectively. Table 2 lists the adopted V_∞ and R_{RC} for individual galaxies.

2.3. Galaxy Properties

We summarize the properties of the selected galaxies in Table 2. The systemic redshifts of the galaxies are spectroscopically determined from the optical emission lines either from the new MMT spectroscopy or from previous work, and we specify the references in the Table. Sections 2.3.1 and 2.3.2 describe the galaxy disk geometry and the stellar and halo masses, respectively. Then, we discuss the galaxy environments in Section 2.3.3.

2.3.1. Galaxy Disk Geometry

We adopted measurements of galaxy disk geometry either from previous work or from the SDSS DR17 catalog (Blanton et al. 2017). Table 2 lists the adopted values and the references for the disk inclination angles i and the azimuthal angles α of the quasar sightlines with respect to the galaxy major axes. Both Martin et al. (2019) and Kacprzak et al. (2019) measured the galaxy disk geometry using high-resolution images: the former obtained K_s -band images from the Keck/NIRC2 camera with Laser Guide Star Adaptive Optics system (Wizinowich et al. 2006), and the latter collected archival HST images from the Advanced Camera for Surveys (ACS) and Wide Field and Planetary Camera 2 (WFPC2). For the remaining galaxies, we used the r -band photometry in the SDSS PhotoObj catalog to derive the azimuthal angle and the inclination angle from the axis ratio³. We show the images of individual galaxies with the same instruments and bandpasses used for measuring the parameters of the disk geometry in Figure 2.

2.3.2. Stellar Masses, Halo Masses, and Virial Radii

The stellar masses M_* of individual galaxies were obtained from previous work and were rescaled to the Chabrier initial mass function (IMF; Chabrier 2003) following Madau & Dickinson (2014). Stellar masses extracted from Martin et al. (2019) were in Chabrier IMF,

³ We applied the Hubble formula (Hubble 1926) with $q_0 = 0.2$.

Table 2. Target Information and Galaxy Properties

Quasar	Galaxy	z_{gal}	$\log M_{\star}$	$\log M_{\text{vir}}$	r_{vir}	V_{∞}	R_{RC}	i	α	d	d/r_{vir}
(1)	(2)	(3)	(4)	(5)	(6)	(7)	(8)	(9)	(10)	(11)	(12)
J040148–054056	J040150–054047	0.21966	9.9 ^a	11.6	168	140	4.8	58 ^b	24 ^b	89	0.53
J080704+360353	J080702+360141	0.088061	10.9 ^c	12.7	426	250	1.4	71 ^b	32 ^b	231	0.54
J084349+261910	J084356+261855	0.11284	10.5 ^c	12.1	261	190	1.5	55 ^b	42 ^b	184	0.71
J085215+171143	J085215+171137	0.16921 ^d	9.8 ^d	11.5	162	200	2.7	77 ^d	23 ^d	20	0.12
J091954+291408	J091954+291345	0.23288 ^d	10.5 ^d	12.2	264	250	3.4	73 ^d	15 ^d	88	0.34
J094331+053131	J094330+053118	0.353052 ^e	9.4 ^a	10.3	128	105	1.5	44 ^e	8 ^e	99	0.77
J103640+565125	J103643+565119	0.13629 ^d	9.9 ^d	11.6	174	210	1.7	58 ^d	21 ^d	58	0.33
J104116+061016	J104117+061018	0.442173 ^e	10.3	12.0 ^e	203	320	1.2	50 ^e	4 ^e	57	0.28
J113910–135043	J113911–135108	0.204194 ^e	10.1	11.7 ^e	184	175	2.4	82 ^e	6 ^e	96	0.52
J113910–135043	J113909–135053	0.319255 ^e	10.2	11.9 ^e	197	205	2.9	83 ^e	39 ^e	77	0.39
J123335+475800	J123338+475757	0.22171	10.6 ^a	12.2	267	225	1.5	74 ^b	5 ^b	141	0.53
J132222+464546	J132222+464546	0.214431 ^e	10.6 ^a	12.2	277	180	1.8	58 ^e	14 ^e	40	0.15
J135522+303324	J135521+303320	0.20690 ^d	9.8 ^d	11.5	157	155	2.8	72 ^d	2 ^d	78	0.50
J142501+382100	J142459+382113	0.21295 ^d	10.2 ^d	11.7	190	190	2.2	61 ^d	7 ^d	83	0.44
J154741+343357	J154741+343350	0.18392 ^d	10.0 ^d	11.6	173	175	1.6	59 ^d	4 ^d	26	0.15
J155504+362847	J155505+362848	0.18926 ^d	10.1 ^d	11.7	188	255	3.6	55 ^d	45 ^d	35	0.19
J160951+353843	J160951+353838	0.28940 ^d	9.9 ^d	11.6	164	45	2.7	65 ^d	25 ^d	25	0.15
J225357+160853	J225400+160925	0.390013 ^e	10.5	12.2 ^e	238	175	3.3	76 ^e	24 ^e	284	1.19

NOTE— (1) Name of the quasar. (2) Name of the galaxy. (3) Galaxy systemic redshift. (4) Galaxy stellar mass, rescaled to Chabrier IMF when necessary following [Madau & Dickinson \(2014\)](#). (5) Halo mass, derived using the stellar mass–halo mass relation in [Behroozi et al. \(2010\)](#) except for those adopted from [Kacprzak et al. \(2019\)](#). (6) Halo virial radius, defined by the overdensity in [Bryan & Norman \(1998\)](#) with respect to the critical density evaluated at the galaxy systemic redshift. (7) Asymptotic rotation speed of the galaxy disk. (8) Turnover radius from the arctangent rotation curve model. (9) Inclination angle of galactic disk. (10) Azimuthal angle, the angle between the quasar sightline and the galaxy major axis. (11) Sightline impact parameter, the projected distance between the centers of the galaxy and quasar. (12) Sightline impact parameter normalized by the halo virial radius.

^a Adopted from [Werk et al. \(2012\)](#). Galaxy stellar masses are rescaled from Salpeter to Chabrier IMF.

^b Derived from SDSS DR17 PhotoObj catalog for *r*-band images. Inclination angle of the galactic disk is calculated from the disk axis ratio using the Hubble formula ([Hubble 1926](#)) with $q_0 = 0.2$. Azimuthal angle of the quasar sightline is calculated from the galaxy major-axis position angle in the catalog.

^c Adopted from [Heckman et al. \(2017\)](#). Galaxy stellar masses are rescaled from Kroupa to Chabrier IMF.

^d Adopted from [Martin et al. \(2019\)](#).

^e Adopted from [Kacprzak et al. \(2019\)](#). With their halo masses, the stellar masses are re-derived using the stellar mass–halo mass relation from [Behroozi et al. \(2010\)](#).

whereas [Werk et al. \(2012\)](#) assumed the Salpeter IMF ([Salpeter 1955](#)), and [Heckman et al. \(2017\)](#) adopted the Kroupa IMF ([Kroupa 2001](#)) as in the MPA-JHU Value-Added Galaxy Catalog. Then, the halo mass M_{vir} of each galaxy was calculated using the stellar mass–halo mass (SM-HM) relation derived from abundance matching in [Behroozi et al. \(2010\)](#). The virial radius r_{vir} was obtained following [Ho et al. \(2017\)](#) using the overdensity defined by [Bryan & Norman \(1998\)](#).

The above procedures were applied for 14 of the 18 galaxies, for which the stellar masses were derived from

multi-band galaxy photometry using the spectral energy distribution fitting technique. But for four galaxies from [Kacprzak et al. \(2019\)](#), instead of first obtaining the stellar masses and then calculate the halo masses, they derived the halo masses from the *r*-band Vega magnitudes of the galaxies following the method in [Churchill et al. \(2013\)](#) (also see [Ng et al. 2019](#)). We used their halo masses and calculated the stellar masses of the galaxies using the SM-HM relation from [Behroozi et al. \(2010\)](#). Then, we derived the virial radii from the halo masses

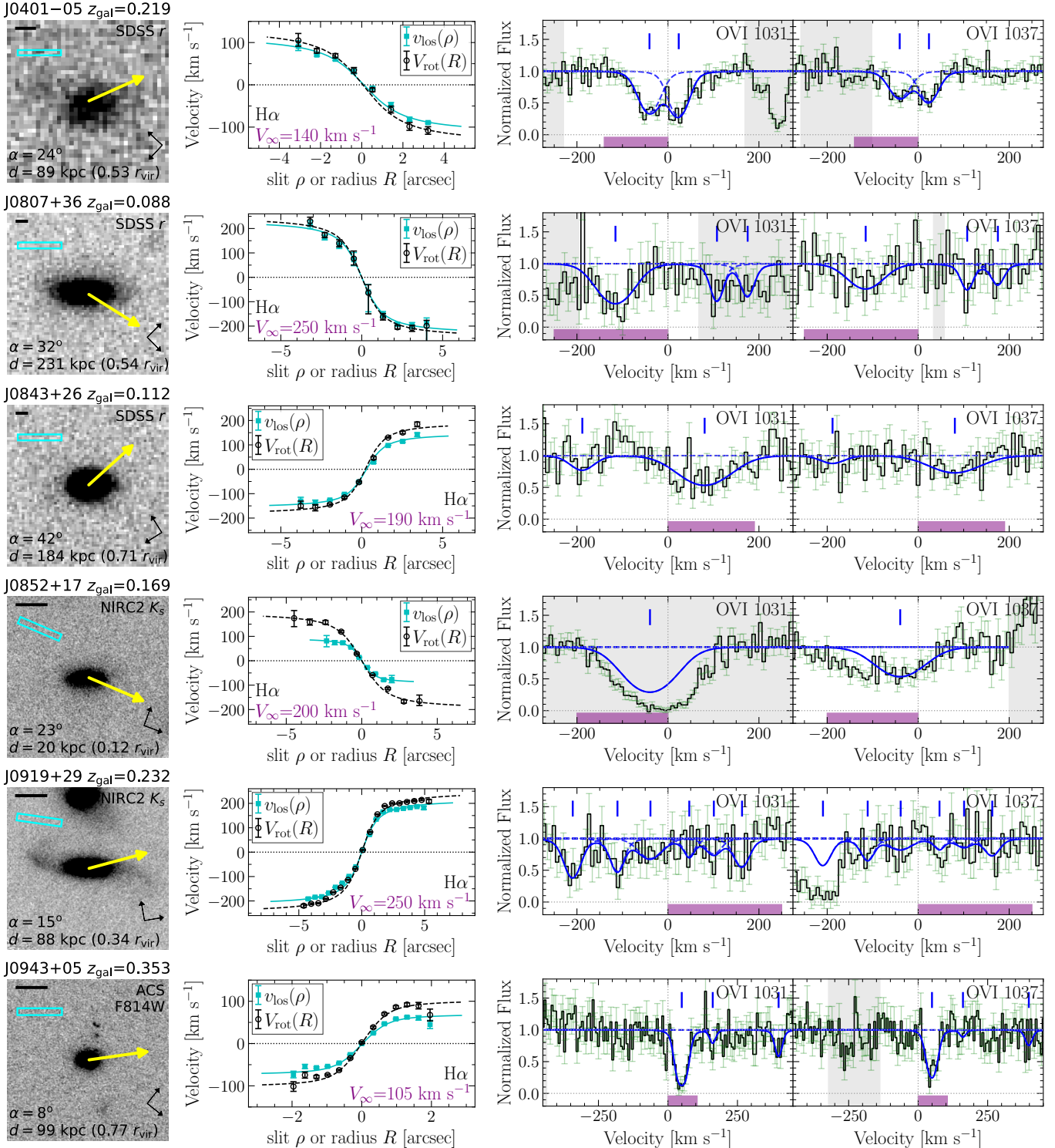
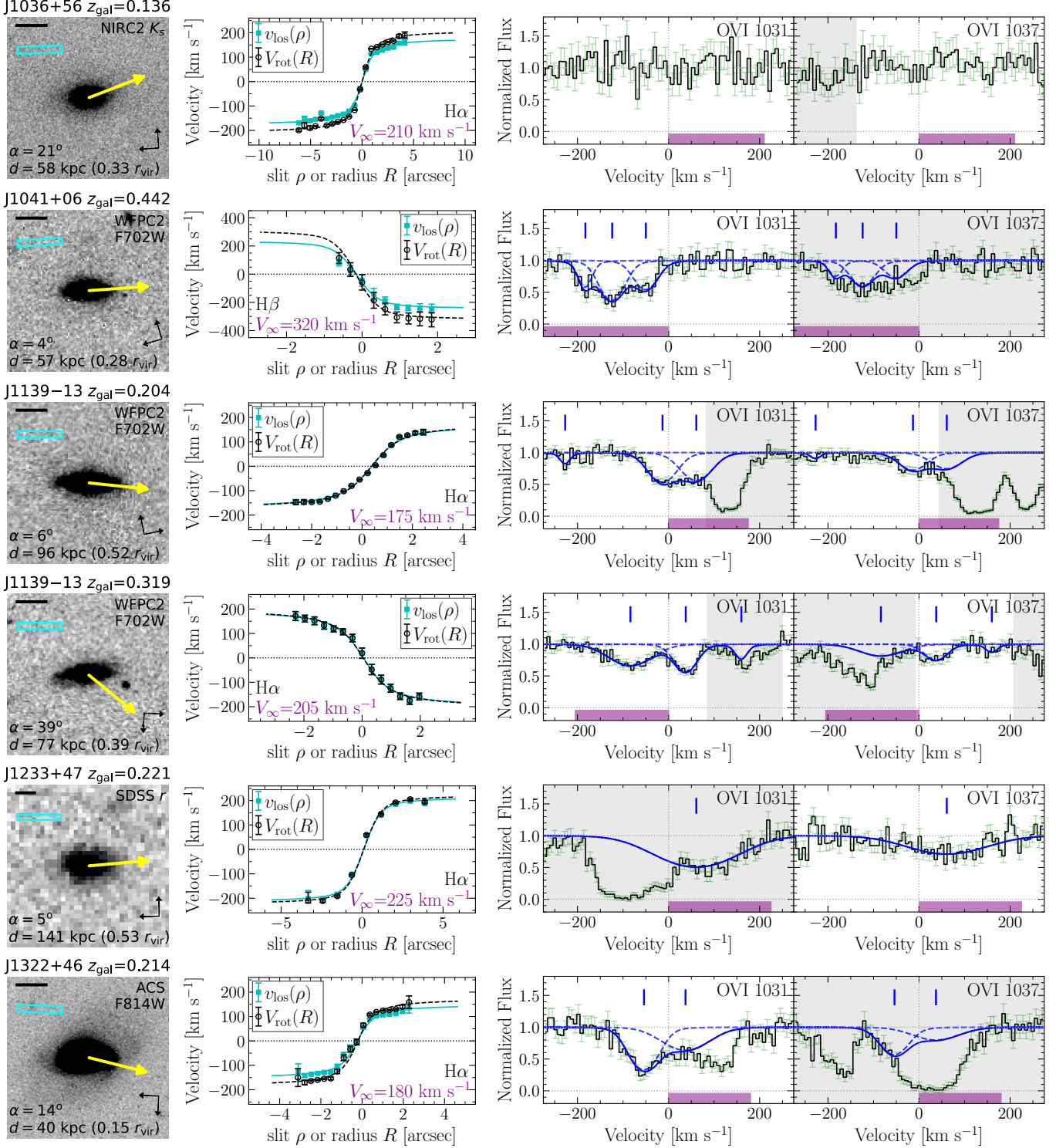
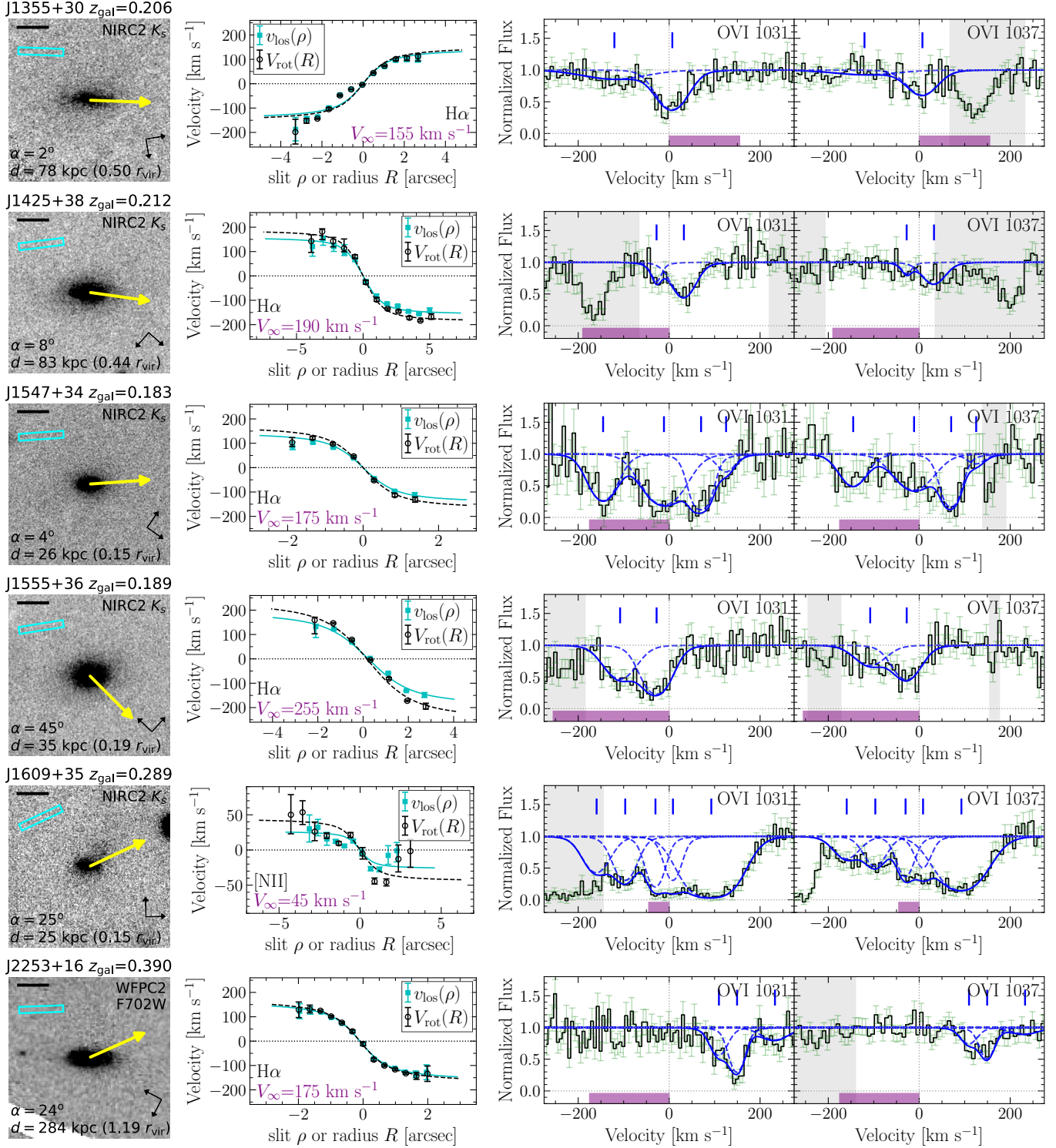


Figure 2. Images of sample galaxies, their rotation kinematics, and O VI absorption measured in the quasar sightlines. *Left:* Images of galaxies. The stamps are $10'' \times 10''$ except for the SDSS r -band images; the black scale bar represents $2''$. Images are oriented with the galaxy major axis aligning with the image x-axis, and the quasar is at the $+x$ direction. The yellow arrow points to the direction of the quasar sightline. The cyan rectangle shows the slit orientation of galaxy spectroscopic observation. *Middle:* Position–velocity diagram (cyan solid squares) and derived rotation curve (black open circles) of galaxy. The bottom labels state the emission line used for deriving the rotation curve (black) and the galaxy asymptotic rotation speed V_∞ (purple). *Right:* O VI $\lambda\lambda 1031, 1037$ absorption lines relative to the galaxy systemic velocity. The blue dashed and solid curves show the fitted Voigt profiles for individual velocity components and the overall O VI absorption, respectively. The blue ticks (top) mark the velocity centroids of individual components. The purple bar (bottom) covers the velocity range between the galaxy systemic velocity and the asymptotic rotation velocity at the quasar side of the galaxy major axis. Grey shaded regions are masked during Voigt profile fitting due to contamination from intervening absorbers at other redshifts.

**Figure 2. (Continued)**

**Figure 2. (Continued)**

following the same procedures as we did for other galaxies.

Table 2 lists the stellar mass, halo mass, and virial radius of individual galaxies, and we label the references of the masses. The median $\log M_\star$ and $\log M_{\text{vir}}$ are 10.14 and 11.72, respectively. The Table also shows the sightline impact parameter normalized by the halo virial radius d/r_{vir} . All except one sightline intersect the galaxies within the virial radius ($d/r_{\text{vir}} < 1$), and most of the sightlines lie within $0.5r_{\text{vir}}$ from the galaxies (also see Figure 1).

2.3.3. Galaxy Environments and Potential Interactions

The group environment of galaxies affect their CGM properties, such as the covering fraction and velocity dispersion, and the CGM becomes kinematically complex (Johnson et al. 2015; Pointon et al. 2017; Nielsen et al. 2018; Dutta et al. 2025). It also leads to uncertainties in identifying the host galaxies associated with the absorption detected in the sightlines. Because we generally lack spectroscopic redshifts for most galaxies in the our fields, we cannot classify the group environment as detailed as in Johnson et al. (2013) and Chen et al. (2020). Nevertheless, using SDSS and SIMBAD (Wenger et al. 2000), we searched for galaxies near our targets to confirm there were no other galaxies with spectroscopic or photometric redshifts comparable to our target galaxies, especially for galaxies with similar r -band magnitudes and/or impact parameters as our targets.

However, the only exception is the target galaxy J091954+291345 at $z = 0.23288$. We found that two red galaxies identified by the SHELS galaxy redshift survey (Geller et al. 2014) have spectroscopic redshifts similar to our target. At the northeast of our target galaxy, a bright red galaxy $4''$ away (17 kpc) has a redshift of 0.23208, i.e., -240 km s^{-1} relative to our galaxy. The other fainter, red galaxy has a redshift of 0.23179, i.e., -327 km s^{-1} , at $8''$ (33 kpc) south of our target. Hence, these three galaxies form a group with velocity differences within a few hundred km s^{-1} . While we present the spectroscopic measurements for this target galaxy and the absorption lines measured in the quasar sightline, we exclude this system from the CGM kinematics analyses in later sections.

For galaxy J160951+353838, it shows a tail-like structure towards the northeast (also see Ho et al. 2017). This tail can be seen towards the upper right in the galaxy image stamp in Figure 2. The galaxy rotation curve also shows irregularity in the same direction. The presence of the tail and the galaxy kinematics together suggest interaction with another galaxy. However, we do not find any bright galaxies with comparable photometric red-

shift that could have interacted with our target galaxy within its virial radius. While the presence of a less massive galaxy or satellite potentially explains the irregular galaxy morphology and kinematics, because our target is not in a close group as J091954+291345, we do not exclude this galaxy in the CGM kinematics analysis.

2.4. Quasar Spectroscopy with HST/COS

The far-UV (FUV) spectroscopy of the background quasars of individual galaxy–quasar pairs were either from our *HST/COS* program (ID: 15866, PI: Ho) or from archival COS data. These COS spectra were obtained using the medium-resolution grating, G130M and/or G160M, with a spectral resolution of $R \approx 20,000$. Table 3 lists the details of the quasar observations with COS.

For each quasar, the raw data from COS were processed by the CALCOS pipeline (v3.3.9), and the one-dimensional spectra (x1d files) were retrieved from MAST⁴. Custom software was used to align the one-dimensional spectra using the Milky Way absorption lines and coadd the aligned spectra. Because COS FUV spectra were oversampled, the coadded spectra were binned by three pixels to increase the signal-to-noise ratio. Finally, each coadded spectrum was continuum-normalized by fitting the quasar continuum with an Akime Spline at the absorption-free regions using the linetools⁵ python package.

2.5. Absorption-line Measurements: Voigt Profile Fitting and Column-density-weighted Velocity

We identified absorption-line systems within $\pm 500 \text{ km s}^{-1}$ of the systemic velocity of the target galaxies. We modeled individual velocity components with Voigt profiles and adopted the atomic data from Morton (2003). The modeled Voigt profile characterized the velocity centroid v , the line width, i.e., the Doppler parameter b , and the column density N of individual velocity component. Using the VoigtFit python package (Krogager 2018), we convolved the models with the COS line-spread function corresponding to the COS lifetime position when the observation was conducted. We compared the convolved line profiles to the data, and different transitions of the same ionic species were fitted jointly. For each ionic species, we created different sets of models with different number of velocity components,

⁴ <http://archive.stsci.edu>

⁵ <https://github.com/linetools/linetools>

Table 3. New and Archival Quasar Spectroscopy with *HST/COS*

Quasar	Quasar RA (J2000)	Quasar DEC (J2000)	z_{qso}	Grating	Exposure Time (s)	Program ID
J040148–054056	04:01:48.98	−05:40:56.5	0.570	G130M/G160M	5377/5912	11598
J080704+360353	08:07:04.88	+36:03:53.5	0.468	G130M/G160M	5378/8612	13862
J084349+261910	08:43:49.75	+26:19:10.7	0.257	G130M	2194	13862
J085215+171143	08:52:15.34	+17:11:43.8	0.562	G130M	10810	15866
J091954+291408	09:19:54.28	+29:14:08.3	0.722	G130M	4933	15866
J094331+053131	09:43:31.61	+05:31:31.4	0.564	G130M/G160M	3662/3945	11598
J103640+565125	10:36:40.74	+56:51:25.9	1.264	G130M	8641	15866
J104116+061016	10:41:17.16	+06:10:16.8	1.270	G160M	14183	12252
J113910–135043	11:39:10.70	−13:50:43.6	0.557	G130M	7669	12275
J123335+475800	12:33:35.07	+47:58:00.4	0.382	G130M/G160M	3885/4218	11598
				G130M	2044	13033
J132222+464546	13:22:22.67	+46:45:35.2	0.374	G130M/G160M	3902/4249	11598
				G130M	2044	13033
J135522+303324	13:55:22.89	+30:33:24.7	0.382	G130M	8092	15866
J142501+382100	14:25:01.46	+38:21:00.5	1.145	G130M	8122	15866
J154741+343357	15:47:41.88	+34:33:57.3	0.928	G130M	5197	15866
J155504+362847	15:55:04.39	+36:28:47.9	0.714	G130M/G160M	5151/6030	11598
J160951+353843	16:09:51.81	+35:38:43.7	0.828	G130M	10639	15866
J225357+160853	22:53:57.74	+16:08:53.5	0.859	G130M/G160M	4473/4514	13398

and the best-fit solution of each model set was determined using a χ^2 minimization algorithm. Finally, we adopted the best-fit model that required the minimum number of velocity components to produce a reasonable fit and with the reduced- χ^2 value closed to one.

The right column of Figure 2 shows the O VI absorption lines relative to the systemic redshifts of individual target galaxies. The fitted Voigt profiles of individual velocity components and the overall O VI absorption are shown in blue dashed and solid curves, respectively, and the blue ticks (top) mark the velocity centroids of individual components. Table 4 lists the parameters of the Voigt profiles of the fitted O VI absorption.⁶ Only the J103640+565125 sightline did not detect O VI around the target galaxy. In that case, we list the 2σ column density upper limit; this was derived from the linear section of the curve-of-growth and the upper limit of the rest-frame equivalent width of O VI 1031, measured using a velocity window that was three times the resolution element centered at the galaxy systemic velocity.

For each sightline, we calculate the column-density-weighted velocity $\langle v \rangle_w$ of the overall absorption. Using the results from Voigt profile fitting, we perturb the fitted velocity centroid and column density of each velocity component by adding a random value within their $1-\sigma$ error bars, and we repeat this process 1000 times. During the i -th iteration, we determine the weighted velocity $\langle v \rangle_{w,i}$ by

$$\langle v \rangle_{w,i} = \frac{\sum_j N_j v_j}{\sum_j N_j}, \quad (4)$$

where j indicates the j -th velocity component, and v_j and N_j represent the perturbed velocity centroid and column density, respectively. From the resultant distribution of the weighted velocity, we adopt the median as the column-density-weighted velocity and the 68% confidence interval as the uncertainties. We show the O VI column-density-weighted velocity $\langle v_{\text{O VI}} \rangle_w$ for each sightline in the rightmost column of Table 4.

3. CGM KINEMATICS AND GALAXY DISK ROTATION

With our sample of quasar sightlines near the major axes of galaxies, we examine the relationship between CGM kinematics and galaxy disk rotation. Section 3.1 and Section 3.2 focus on the O VI CGM and the low-ionization-state gas, respectively. In Section 3.3, we then compare the kinematics of the low ions and O VI

⁶ The Figures of the fitted line profiles of other ions and Voigt profile parameters are shown in Figure 11 and Table 6, respectively, in the Appendix.

Table 4. Results from Voigt Profile Fitting of O VI Absorption

Quasar	Galaxy	z_{gal}	v	b	$\log N_{\text{OVI}}$	$\langle v_{\text{O VI}} \rangle_w$
(1)	(2)	(3)	(4)	(5)	(6)	(7)
J040148–054056	J040150–054047	0.21966	-40.6 ± 4.2	26.2 ± 6.2	14.26 ± 0.06	$-6.8^{+2.3}_{-2.3}$
			23.6 ± 3.0	23.1 ± 4.3	14.31 ± 0.06	
J080704+360353	J080702+360141	0.088061	-115.4 ± 7.7	46.4 ± 11.4	14.43 ± 0.08	$4.3^{+15.8}_{-20.1}$
			107.7 ± 10.5	12.0 ± 17.5	14.12 ± 0.23	
			175.2 ± 12.1	12.9 ± 21.6	13.99 ± 0.29	
J084349+261910	J084356+261855	0.11284	-188.3 ± 15.1	30.6 ± 22.7	13.70 ± 0.19	$34.1^{+10.6}_{-13.3}$
			80.5 ± 8.9	70.3 ± 12.7	14.37 ± 0.05	
J085215+171143	J085215+171137	0.16921	-39.5 ± 9.2	64.9 ± 15.5	14.64 ± 0.07	$-39.2^{+5.8}_{-6.6}$
J094331+053131	J094330+053118	0.353052	49.6 ± 1.8	20.1 ± 2.6	14.64 ± 0.08	$93.1^{+7.9}_{-7.0}$
			161.1 ± 4.4	11.0 ± 10.0	13.32 ± 0.31	
			397.9 ± 4.4	13.6 ± 7.0	13.75 ± 0.12	
J103640+565125	J103643+565119	0.13629	$\leq 13.2^{\dagger}$...
J104116+061016	J104117+061018	0.442173	-182.7 ± 5.0	15.8 ± 7.7	13.82 ± 0.16	$-111.7^{+4.9}_{-4.4}$
			-123.9 ± 4.8	30.9 ± 10.7	14.28 ± 0.09	
			-49.9 ± 7.5	30.2 ± 9.8	14.06 ± 0.12	
J113910–135043	J113911–135108	0.204194	-227.0 ± 8.7	10.5 ± 19.8	13.26 ± 0.32	$6.5^{+12.5}_{-13.4}$
			-13.2 ± 14.9	36.7 ± 18.6	14.14 ± 0.20	
			61.0 ± 11.9	40.7 ± 29.7	14.12 ± 0.29	
J113910–135043	J113909–135053	0.319255	-83.9 ± 4.3	59.8 ± 6.9	14.11 ± 0.04	$-9.7^{+5.0}_{-4.8}$
			37.7 ± 2.0	29.4 ± 3.4	14.01 ± 0.04	
			159.8 ± 6.6	14.3 ± 10.8	13.45 ± 0.16	
J123335+475800	J123338+475757	0.22171	60.9 ± 11.0	112.2 ± 15.3	14.59 ± 0.05	$60.8^{+7.7}_{-7.2}$
J132222+464546	J132222+464546	0.214431	-54.1 ± 6.2	36.8 ± 7.1	14.39 ± 0.10	$-18.6^{+8.2}_{-7.5}$
			37.3 ± 22.0	64.8 ± 22.4	14.19 ± 0.17	
J135522+303324	J135521+303320	0.20690	-120.5 ± 28.6	90.8 ± 44.6	13.86 ± 0.21	$-22.9^{+7.7}_{-10.2}$
			7.0 ± 4.0	38.7 ± 5.6	14.36 ± 0.05	
J142501+382100	J142459+382113	0.21295	-27.7 ± 5.9	7.3 ± 13.0	13.62 ± 0.34	$19.3^{+5.5}_{-6.5}$
			32.4 ± 4.7	27.9 ± 8.2	14.18 ± 0.07	
J154741+343357	J154741+343350	0.18392	-145.3 ± 4.8	33.3 ± 7.5	14.47 ± 0.07	$14.0^{+11.6}_{-10.9}$
			-11.4 ± 9.4	49.5 ± 13.6	14.68 ± 0.09	
			70.1 ± 5.1	18.3 ± 9.7	14.99 ± 0.23	
			125.3 ± 16.0	20.8 ± 25.9	13.71 ± 0.38	
J155504+362847	J155505+362848	0.18926	-27.5 ± 6.8	35.8 ± 7.4	14.53 ± 0.09	$-55.7^{+6.5}_{-5.8}$
			-107.9 ± 13.9	41.2 ± 16.6	14.26 ± 0.16	
J160951+353843	J160951+353838	0.28940	-159.5 ± 17.4	32.6 ± 28.9	14.24 ± 0.29	$23.9^{+7.3}_{-8.2}$
			-96.5 ± 10.0	26.5 ± 14.1	14.36 ± 0.21	
			-30.0 ± 6.7	18.4 ± 1.7	14.50 ± 0.19	
			8.4 ± 9.1	17.6 ± 16.1	14.29 ± 0.29	
			92.8 ± 5.6	57.8 ± 5.9	15.10 ± 0.04	
J225357+160853	J225400+160925	0.390013	109.6 ± 16.0	21.3 ± 16.4	13.91 ± 0.34	$151.7^{+7.2}_{-7.6}$
			149.5 ± 6.5	17.6 ± 7.8	14.24 ± 0.17	
			232.7 ± 14.0	38.0 ± 23.8	13.67 ± 0.19	
Excluded from O VI kinematics analysis due to group environment						
J091954+291408	J091954+291345	0.23288	-209.4 ± 4.9	16.2 ± 8.9	14.21 ± 0.19	$-56.7^{+17.3}_{-17.1}$
			-110.9 ± 5.1	12.0 ± 9.0	14.04 ± 0.19	
			-38.4 ± 11.7	28.8 ± 20.7	13.85 ± 0.17	
			46.9 ± 11.4	7.3 ± 22.0	13.61 ± 0.23	
			100.9 ± 16.3	16.1 ± 37.8	13.58 ± 0.41	
			162.9 ± 9.7	15.2 ± 16.7	13.93 ± 0.16	

† The 2σ upper limit measured from O VI 1031.

NOTE— (1) Name of the quasar. (2) Name of the galaxy. (3) Galaxy systemic redshift. (4) Velocity centroid of individual component. (5) Line width, i.e., Doppler parameter, of the velocity component. (6) Logarithm of the column density of the velocity component. (7) Column-density-weighted velocity.

detected in individual sightlines. In our analyses, we exclude galaxy J091954+291345 due to its close group environment (Section 2.3.3) and focus on the remaining 17 galaxy–quasar pairs.

3.1. Kinematics of O VI Gas

Among the 17 galaxy–quasar pairs, all sightlines except J103640+565125 have detected O VI around the host galaxies. Figure 3 compares the kinematics of the O VI gas and that of the galaxy disk rotation. The circles and the dashed curves represent the velocity centroids of individual O VI velocity components and the galaxy rotation curves, respectively. With similar numbers of O VI velocity components that corotate (21) and counter-rotate (15) with the disk (Table 5), it seems to suggest a lack of correlation between disk rotation and the kinematics of individual O VI velocity components. However, except for the sightline at the highest impact parameter of 284 kpc, the column-density-weighted velocities (black crosses) suggest that the bulk of O VI gas either corotates with the disk or is consistent with being at the systemic velocity of the host galaxies (within the grey band).⁷ In other words, we rarely found sightlines with net counter-rotating O VI absorbers.

In the bottom panel of Figure 3, we normalized the velocities and impact parameters by the asymptotic rotation speeds and virial radii of the galaxies, respectively. The velocity centroids of most O VI components (34 out of 41) are smaller than the asymptotic rotation speed, i.e., $|v_{\text{O VI}}/V_\infty| < 1$. Sightlines with O VI components exceeding V_∞ typically have large impact parameters of $\geq 0.5r_{\text{vir}}$. The only exception is the sightline around host galaxy J160951+353838, but this galaxy has a tail-like structure and an abnormally low asymptotic rotation speed of 45 km s^{-1} (Section 2.3.3). This explains the high $|v_{\text{O VI}}/V_\infty|$ values even though the measured O VI velocities in km s^{-1} are comparable to those in other sightlines.

3.2. Corotation of the Low-ionization-state Gas with the Disk

Low-ionization-state ions trace cooler gas compared to O VI due to their lower ionization potentials (IP), e.g., Si II and Si III with IP of 8.2 eV and 16.3 eV, respectively, compared to 113.9 eV for producing O VI. For our sample, only 13 sightlines have COS spectra that

⁷ Velocities smaller than the measurement uncertainties of the galaxy redshift of 25 km s^{-1} are considered as being consistent with the galaxy systemic velocity.

Table 5. Classification of O VI Velocity Components

O VI Category	Kinematics Class	$n_{\text{comp,O VI}}$	Ratio
(1)	(2)	(3)	(4)
All Sightlines (exclude J0919+29)			
All	Any	41	...
	Corotate	21	0.51
	Systemic Velocity	5	0.12
	Counter-rotate	15	0.37
Sightlines with Si II and Si III Spectral Coverage ($n_{\text{comp,O VI}} = 29$) [†]			
All	Any	29	...
	Corotate	16	0.55
	Systemic Velocity	3	0.10
	Counter-rotate	10	0.34
With Si II match	Any	10	...
	Corotate	9	0.90
	Systemic Velocity	1	0.10
	Counter-rotate	0	0
No Si II match	Any	19	...
	Corotate	7	0.37
	Systemic Velocity	2	0.11
	Counter-rotate	10	0.53
With Si III match	Any	14	...
	Corotate	10	0.71
	Systemic Velocity	2	0.14
	Counter-rotate	2	0.14
No Si III match	Any	15	...
	Corotate	6	0.40
	Systemic Velocity	1	0.07
	Counter-rotate	8	0.53

[†]The sightlines either have spectral coverage for both Si II and Si III simultaneously or neither.

NOTE— (1) Category of O VI velocity components. (2) Classification of O VI velocity components based on their Doppler sign relative to the disk rotation at the quasar side of the galaxy disk. (3) Number of O VI velocity components. (4) The ratio of the number of O VI velocity components between the kinematics class and the total within the same O VI category.

cover the redshifted wavelengths of Si II⁸ and Si III of the host galaxies, including the J103640+565125 sightline without O VI detection. Among these 13 sightlines, Si III exhibits a higher detection rate compared to Si II, with 7 and 11 sightlines showing Si II and Si III detection, respectively.

Figure 4 compares the kinematics of the Si II (left) and Si III (right) gas to disk rotation. Except for the sight-

⁸ We focus on the Si II $\lambda\lambda 1190, 1193$ and Si II $\lambda 1260$ transitions, because other Si II transition lines within the spectral coverage are either too weak to be detected or blended with other absorption lines.

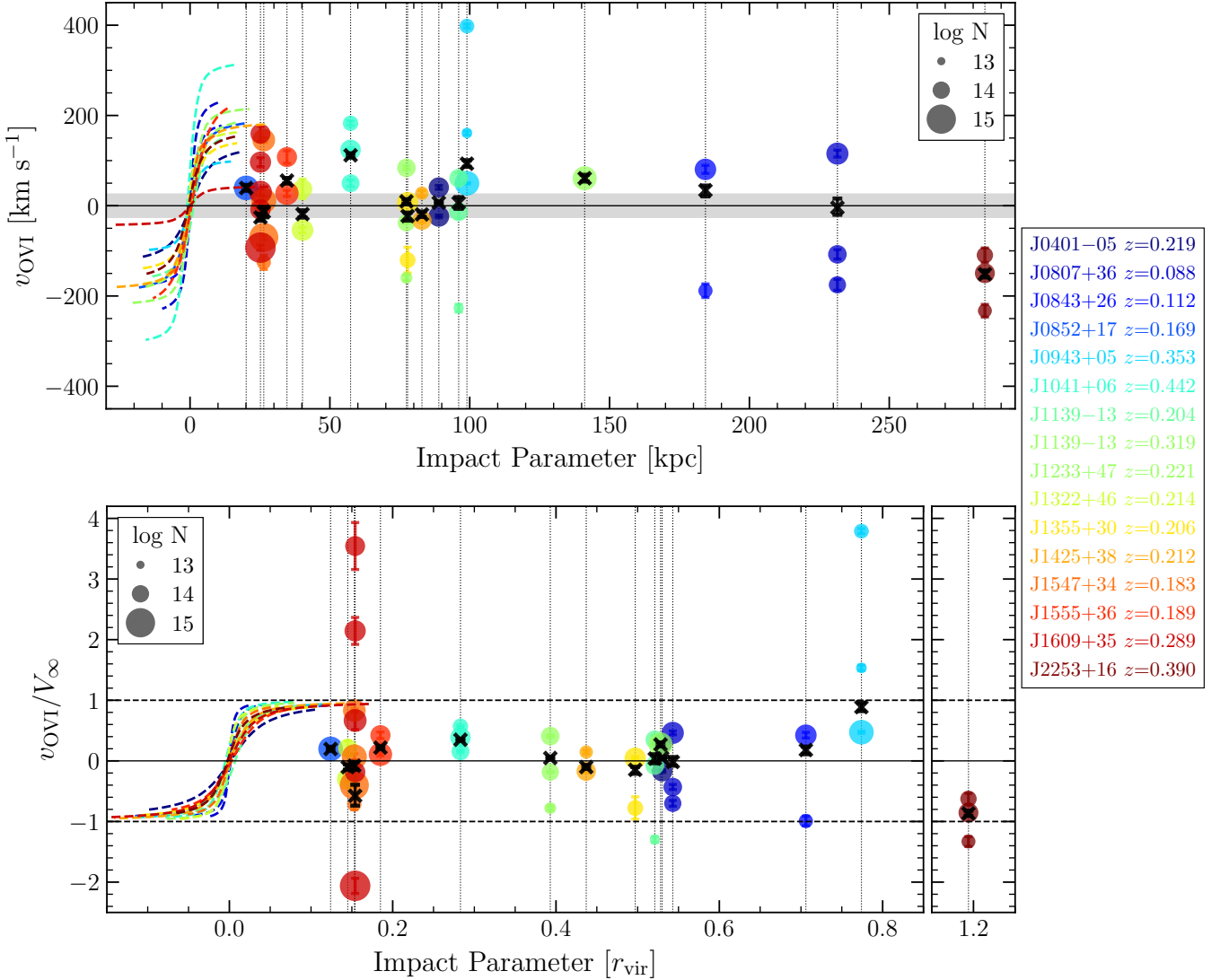


Figure 3. Comparison of O VI gas kinematics to galaxy disk rotation. The curves represent the rotation curves of individual galaxies. Each circle indicates the velocity centroid of individual O VI velocity component, and the marker size scales with the column density. For the purpose of uniformity in this figure, galaxy rotation curves are defined with a positive velocity at the quasar side of the galaxy major axis. In the top panel, the vertical and horizontal axes show the line-of-sight O VI velocity $v_{\text{O VI}}$ and quasar sightline impact parameter, and the bottom panel normalized the axes by the galaxy asymptotic rotation speed V_∞ and virial radius r_{vir} , respectively. The grey shaded region indicates the velocity range where the gas is indistinguishable from being at the systemic velocity of the galaxy ($\pm 25 \text{ km s}^{-1}$). Each black cross shows the column-density-weighted O VI velocity $\langle v_{\text{O VI}} \rangle_w$ of each sightline, and the associated error is typically comparable or smaller than the size of the cross. The only net counter-rotating O VI absorber (i.e., $\langle v_{\text{O VI}} \rangle_w$ and disk rotation have opposite Doppler sign and $|\langle v_{\text{O VI}} \rangle_w| > 25 \text{ km s}^{-1}$) is detected at the sightline with the highest impact parameter of 284 kpc ($1.19 r_{\text{vir}}$).

line at 184 kpc from galaxy J084356+261855, six out of the seven Si II-detected sightlines show net corotating Si II absorption, and only two (out of 21) Si II velocity components counter-rotate with the disk. Net counter-rotating Si III absorbers are also rare, but the fraction of Si III velocity components that counter-rotate with the disk becomes higher compared to that of Si II.

Figure 5 shows the fraction of non-counter-rotating velocity components of Si II, Si III, and O VI, i.e., the gas

either corotates with the disk or consistent with being at the systemic velocity of the host galaxy.⁹ Considering all sightlines regardless of their impact parameters (“All”), Si II has the highest fraction of non-counter-

⁹ Both black hatched and maroon filled histograms represent O VI, but the former includes all sightlines, whereas the latter only includes the 13 sightlines with Si II and Si III spectral coverage.

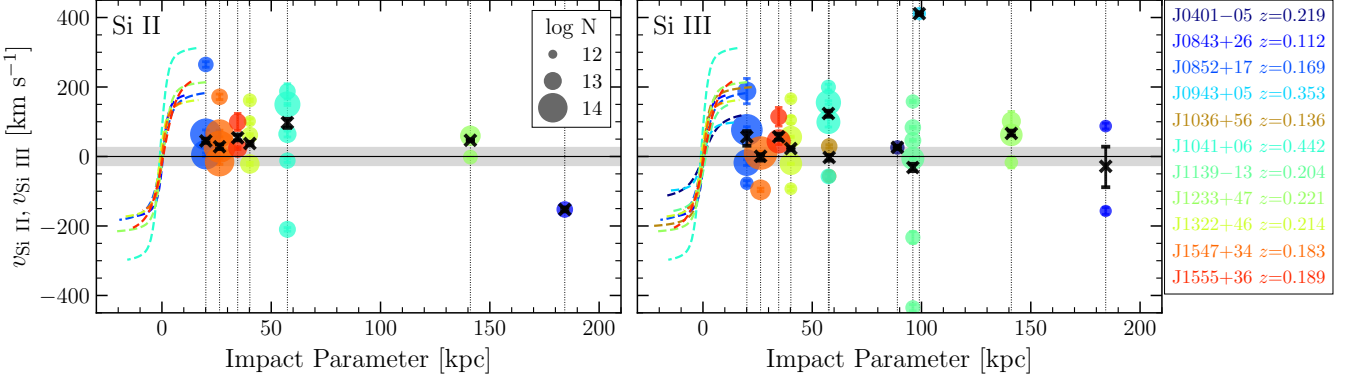


Figure 4. Comparison of Si II and Si III gas kinematics to galaxy disk rotation. This figure is analogous to the top panel of Figure 3, but each circle in the left and right panels represents the velocity centroid of individual Si II and Si III velocity component, respectively. Different colors correspond to individual sightlines the same way as in Figure 3. J1036+56 is added; it is not shown in Figure 3 due to O VI non-detection. Among the 13 sightlines with spectral coverage of Si II and Si III, 7 and 11 sightlines have detected Si II and Si III, respectively. Net counter-rotating Si II and Si III absorbers are rare. As for individual velocity components, while very few of them counter-rotate with the disk, Si III, which has a higher ionization than Si II, shows a higher counter-rotation rate.

rotating velocity components of 90%. The fraction drops with increasing ionization potential, for which only 75% (60%) of the Si III (O VI) velocity components are not counter-rotating. If we only focus on the sightlines with impact parameters below 100 kpc, the fraction of non-counter-rotating velocity components for all three ions become comparable (between 75% and 95%). However, in sightlines beyond 100 kpc from the host galaxies, O VI shows a significantly lower non-counter-rotating fraction compared to Si II and Si III in the same impact parameter range and also compared to the O VI detected at small impact parameters. Therefore, in contrast to low-ionization-state gas that rarely counter-rotates with the disk, whether individual velocity components of the O VI gas counter-rotate depends on the sightline impact parameter, with sightlines at larger impact parameters more frequently detect counter-rotating O VI gas.

3.3. Comparison Between O VI and Low-ionization-state Gas Kinematics

Sections 3.1 and 3.2 have shown that the low-ionization-state gas traced by Si II and Si III rarely counter-rotate with the disk compared to O VI, suggesting that O VI gas exhibits different kinematics compared to the lower ionization counterparts. In Figure 6, we compare the Voigt profile fits of O VI to those of Si II and Si III measured in individual sightlines.¹⁰ We arrange the panels in increasing impact parameter of the

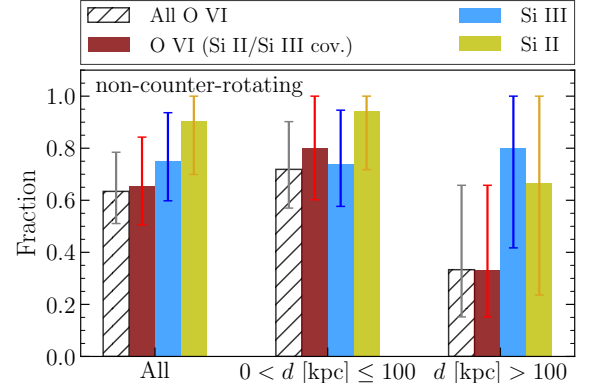


Figure 5. Fraction of non-counter-rotating velocity components of Si II, Si III, and O VI compared to the galaxy disk rotation. Different colors represent different ions; “All O VI” represents all O VI velocity components, whereas “O VI (Si II/Si III cov.)” only shows the O VI components in the 13 sightlines with Si II and Si III spectral coverage. Regardless of the sightline impact parameter (left), Si II shows the highest fraction of non-counter-rotating velocity components. By dividing the sightlines into impact parameter bins of below (middle) and above 100 kpc (right), O VI shows a higher non-counter-rotating fraction in sightlines with smaller impact parameters compared to sightlines further away.

quasar sightlines. First, Si II and Si III are more frequently detected in sightlines at low impact parameters, and the two sightlines beyond 200 kpc from the host galaxies neither detect Si II nor Si III. Secondly, the line profiles of different ions have complex component structures, especially sightlines closer to the galaxies tend to have more velocity components. While some O VI components have velocities comparable to their low-ionization-state counterparts, some do not affiliate

¹⁰ For the J154741+343357 sightline, the Si III absorption-line profile is incomplete, because it falls at the reddest end of the spectrum. The J103640+565125 sightline is not shown due to O VI non-detection.

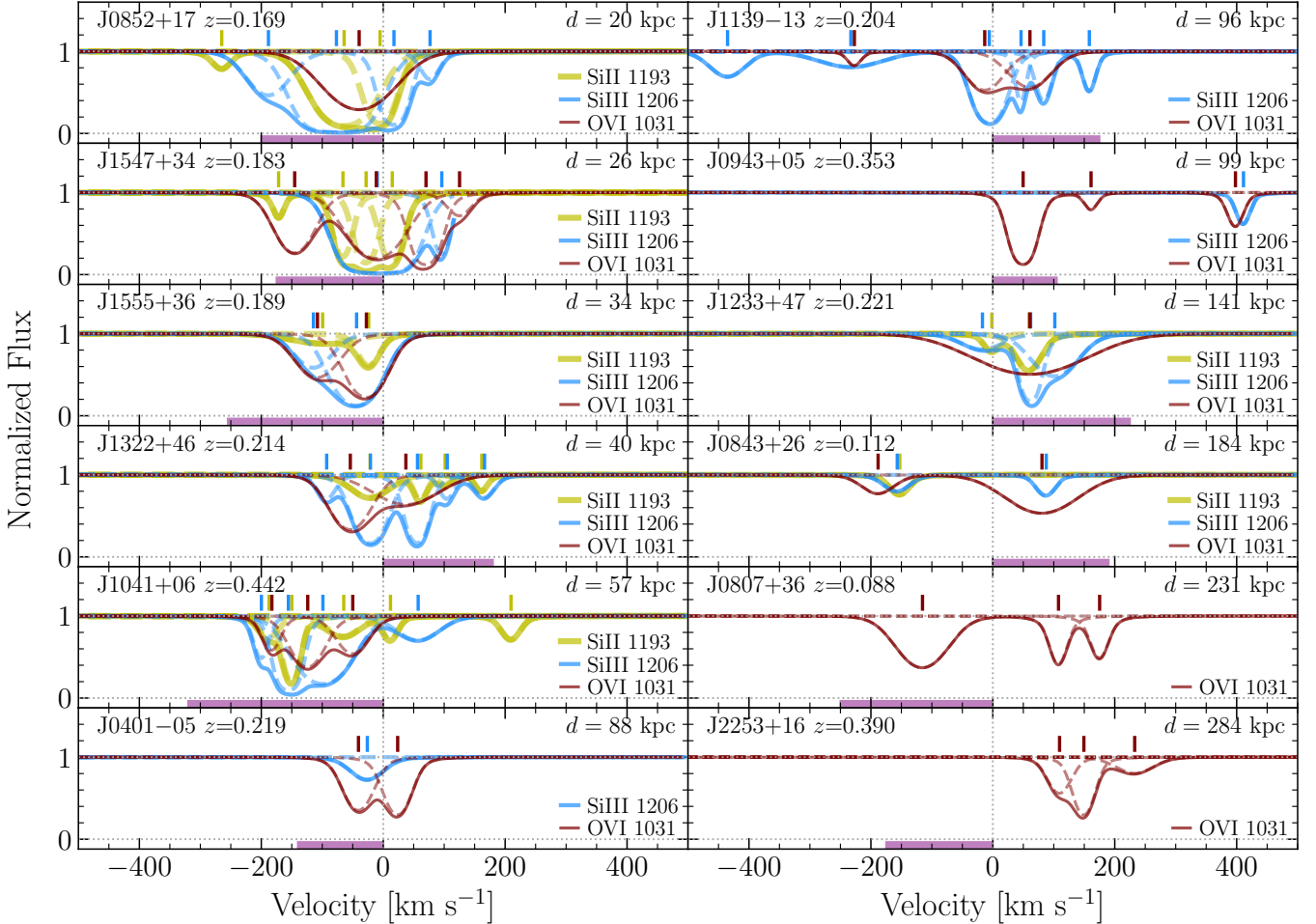


Figure 6. Comparison of Voigt profile fits for all 12 sightlines with O VI (thin maroon) detected and simultaneously with spectral coverage for Si II (thickest yellow) and Si III (thick cyan). Panels are arranged in increasing sightline impact parameter (upper right label). Dashed and solid lines represent individual velocity components and the overall fitted Voigt profile, respectively. Similar to Figure 2, ticks at the top mark the velocity centroids of individual components. The purple bar at the bottom covers the velocity range between the galaxy systemic velocity and the asymptotic rotation velocity at the quasar side of the galaxy major axis. Despite the complex line profile structures, the overall absorption of different ions covers similar velocity ranges.

with the low ions. But regardless, the overall absorption of different ions typically occupy similar velocity ranges.

Motivated by Figure 6 that shows that only some O VI components have velocities comparable to those of the low ions, we examine how the kinematics association between O VI and low ions (or the lackthereof) relates to the comparison of O VI kinematics and disk rotation. In each sightline, we attempt to match individual O VI velocity components with those of Si II and Si III by minimizing the difference of their velocity centroids. We consider an O VI velocity component to be successfully matched with a Si II or Si III component if the velocity difference is under 30 km s^{-1} , a threshold that includes the uncertainties in defining the galaxy systemic veloc-

ity, the wavelength calibration of the COS spectra¹¹, and the typical uncertainty of the velocity centroid from Voigt profile fitting.¹² Each Si II or Si III velocity component can only be matched with one O VI component (and vice versa). Hence, if more than one Si II or Si III component satisfy the matching criteria with O VI, then we select the one with the smallest velocity difference.

¹¹ According to the “Cycle 26 COS/FUV Spectroscopic Sensitivity Monitor (ISR 2020-06)”, the COS wavelength zero point uncertainties are 3 pixels, i.e., $\sim 10 \text{ km s}^{-1}$.

¹² While increasing (decreasing) the 30 km s^{-1} threshold value will increase (reduce) the number of low-ion matched O VI velocity components, it does not affect the main conclusions from the kinematics comparison between O VI components with and without low-ion matches.

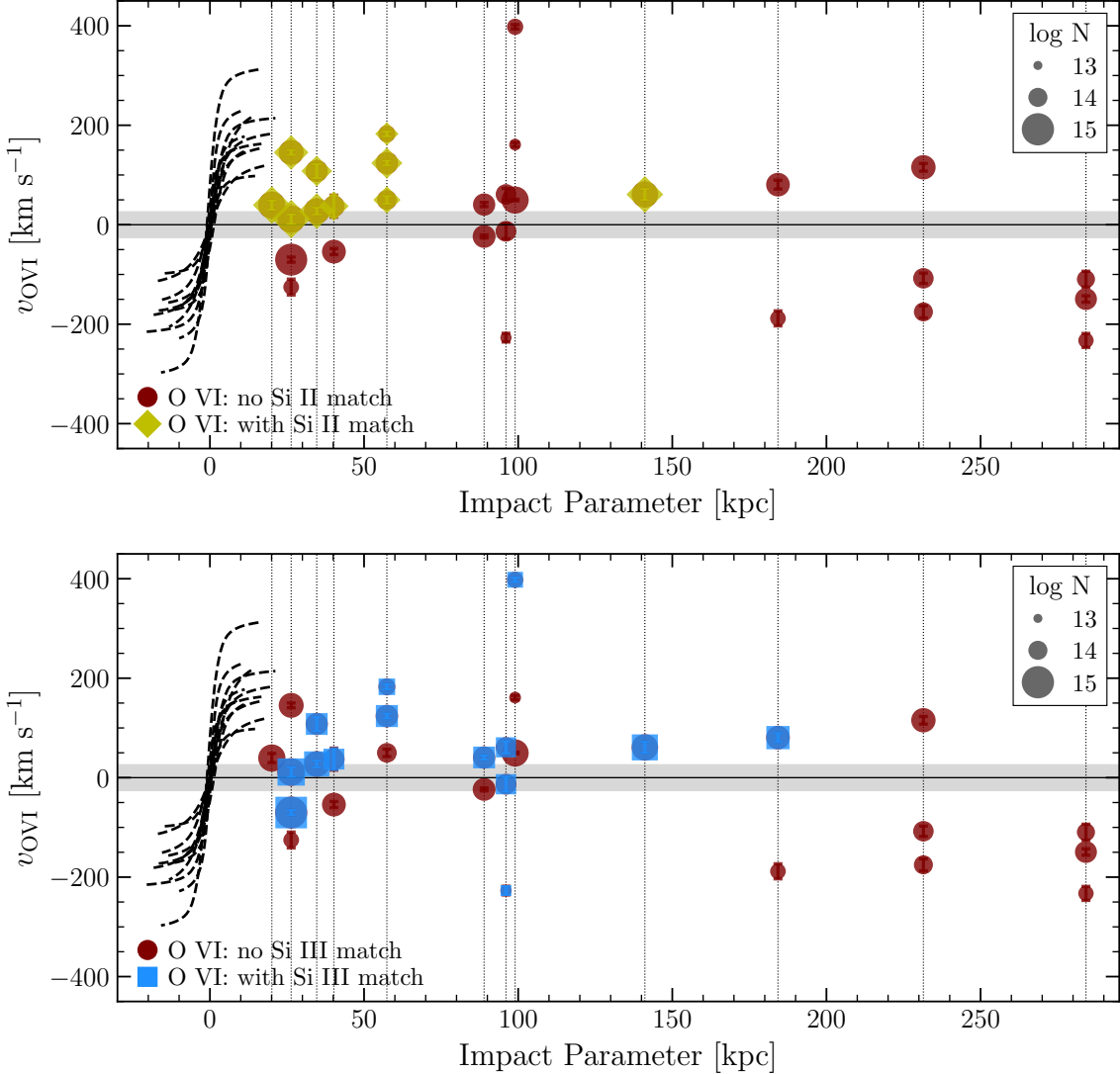


Figure 7. Comparison of O VI gas kinematics with Si II- and Si III-matched velocity components to galaxy disk rotation. Similar to the top panel of Figure 3, but this Figure only shows the sightlines with Si II and Si III spectral coverage. In the top (bottom) panel, the O VI velocity components successfully matched with Si II (Si III) are highlighted in yellow diamonds (cyan squares). Maroon circles represent the unmatched O VI velocity components. Most of the Si II- or Si III-matched O VI velocity components corotate with the galaxy disk, and none of the Si II-matched components counter-rotates.

Analogous to Figure 3, Figure 7 compares the O VI kinematics with galaxy disk rotation by showing the 12 sightlines with O VI detection and spectral coverage of Si II and Si III. Each marker represents the velocity centroid of an O VI component, and the yellow diamonds (top) and cyan squares (bottom) highlight the Si II- and Si III-matched O VI components, respectively. Both panels clearly show that Si II- or Si III-matched O VI velocity components rarely counter-rotate with the galaxy disk (also see Table 5). In fact, none of the Si II-matched O VI velocity components counter-rotates (0/10), in contrast to the 10/19 (53%) no-Si II-matched O VI components that counter-rotate with the disk.

While counter-rotating Si III-matched O VI components exist (2/14; 14%), that occurs less frequently compared to the O VI components without a Si III match (8/15; 53%).

Not only the Si II- and Si III-matched O VI components rarely counter-rotate, but they also preferentially corotate with the disk instead of being at the galaxy systemic velocity. Specifically, 9/10 (90%) of the Si II-matched O VI components corotate with the disk in contrast to only 7/19 (37%) of the O VI components without a Si II match. The contrast becomes less prominent for Si III. But still, a higher fraction (10/14; 71%) of the Si III-matched O VI components corotate

with the disk compared to that of the no-Si III-matched O VI components (6/15; 40%). Our results show that the O VI velocity components with and without low-ion matches have different kinematics properties and possibly trace gas that resides at different 3D distances from the host galaxies. Because O VI velocity components with matched low-ion are more likely to corotate with the disk, a plausible scenario is that the gas resides on an extended disk plane. We further discuss the implications of our results in Section 4.

4. DISCUSSION

In Section 3, we have presented the kinematics of the O VI gas and compared that with galaxy disk rotation and the kinematics of low-ionization-state gas traced by Si II and Si III. While individual velocity components of the O VI gas do not seem to correlate with the galaxy disk rotation, the column-density-weighted velocity of O VI suggests that the bulk of O VI gas rarely counter-rotate with the disk (Figure 3). We have also matched velocity components of O VI with Si II and Si III by minimizing the differences of their velocity centroids. This analysis has shown that the Si II- or Si III-matched O VI velocity components more frequently corotate with the disk compared to velocity components that cannot be matched with the low ions (Figure 7). In this Section, we discuss the implications and interpretation of these results.

4.1. Location of the Multiphase Gas Traced by O VI, Si II, and Si III

Among the 12 sightlines with O VI detection and spectral coverage of Si II and Si III, O VI is detected in sightlines out to larger impact parameters compared to the low ions (Figures 3, 4, and 6). This result is commonly found in previous work. While low ions are only detected in the inner CGM out to ~ 100 kpc around star-forming galaxies, O VI is detected out to impact parameters of several hundred kpc (see Section 1). This implies that O VI is more spatially extended compared to the low-ionization-state gas that resides in the inner CGM.

In general, quasar absorption-line analysis only produces line-of-sight measurements and do not reveal the location of the absorbing gas in 3D space. However, our kinematics comparison between O VI and low ions provides the clues for distinguishing the location of the detected gas. Figure 7 shows that Si II- and Si III-matched O VI velocity components more frequently corotate with the disk compared to those components without low-ion matches, and most of the matched components are found in sightlines with impact parameters below 100 kpc. This may not seem surprising, because low ions

are often detected in the inner CGM and corotate with the disk, suggesting that the low ions trace the gas residing near the extended disk plane of the galaxy (e.g., Kacprzak et al. 2011; Ho et al. 2017). But with the subset of O VI components having velocities that matched with the low ions and also corotating with the disk, this suggests that these low-ion-matched O VI components trace the gas that is co-spatial with the low ions, i.e., near the extended disk plane in the inner CGM. On the other hand, the unmatched O VI velocity components correspond to gas at the outer CGM.

The interpretation of the location of the absorbing gas explains two results. First, it explains why the Si II- and Si III-matched O VI velocity components are more likely to be corotating with the disk compared to those O VI components without a low-ion match. It also explains the complicated line structures detected in sightlines with small impact parameters (Figure 6), because these sightlines intersect both the inner and outer CGM with different O VI kinematics. Therefore, our results imply that while the outer O VI CGM tends to move randomly, the inner O VI CGM carries angular momentum and corotates with the galaxy disk similar to the low-ionization-state gas.

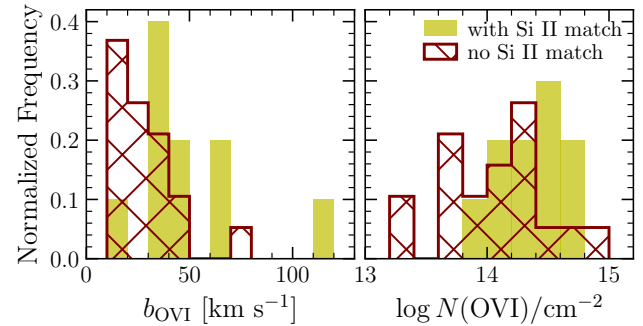


Figure 8. Distribution of Doppler parameter (left) and column density (right) of O VI velocity components with (solid yellow) and without Si II matches (hatched maroon). Performing the KS test on the Doppler parameter rejects the null hypothesis at $\approx 96\%$ that the two O VI populations are drawn from the same distribution, but the null hypothesis cannot be ruled out for the column density measurements.

Furthermore, the O VI velocity components with Si II matches tend to have larger Doppler parameters compared to those without Si II matches. Figure 8 shows the distributions of the Doppler parameter and column density for the two O VI populations. Performing the Kolmogorov-Smirnov (KS) test on the Doppler parameter rules out the null hypothesis at $\approx 96\%$ that the O VI components with and without Si II matches are drawn from the same population distribution. However, the

null hypothesis cannot be rejected for the column density populations. On the other hand, when we repeat the same analysis for the O VI components with and without Si III matches, the null hypothesis cannot be ruled out for both measured quantities. In fact, since Si II-matched O VI components are more likely to be corotating with the disk compared to those without Si II matches, the larger Doppler parameter of the former plausibly suggests that the rotation motion (in addition to turbulence) has broadened the absorption lines. Because the net CGM angular momentum remains roughly constant with radius in 3D space, the rotation velocity is expected to decrease towards the outer CGM. With Si III generally being more spatially extended compared to the lower-ionization Si II counterpart, we expect the O VI components with Si III matches to trace the gas out to larger 3D radii and have lower rotation velocities on average compared to those with Si II matches. As a result, the rotation motion has produced a measurable increase to the absorption-line width of the O VI velocity components with Si II matches but not those with Si III matches, which also explains why the latter have comparable Doppler parameters as the no-Si III-matched O VI components.

4.2. Angular Momentum of the CGM and Radial Infall

While the absorption-line measurements do not reveal where the gas is located along the line of sight, we have argued that some of the O VI velocity components are tracing gas near the extended disk plane of galaxies (Section 4.1). But does the corotating gas have sufficient angular momentum to stay on circular orbits? If not, the gas could be infalling to the galaxy, a plausible scenario that explains the corotating low-ionization-state gas at sub-centrifugal velocities (e.g., Ho et al. 2017; Ho & Martin 2020).

We explore this radial inflow hypothesis by assuming all the non-counter-rotating gas being on the extended disk plane. Then, we calculate the implied galactocentric radii R_{ion} and the circular velocities $V_{c,\text{ion}}$ for individual Si II, Si III, and O VI velocity components. We compare these circular velocities to that required for the gas to stay on circular orbits, assuming the galaxy disks maintain the flat, arctangent rotation curve out to the galactocentric radii. The histograms in Figure 9 show the fractions of Si II, Si III, and O VI velocity components with circular velocities too low to be on circular orbits, i.e., the gas lacks sufficient angular momentum

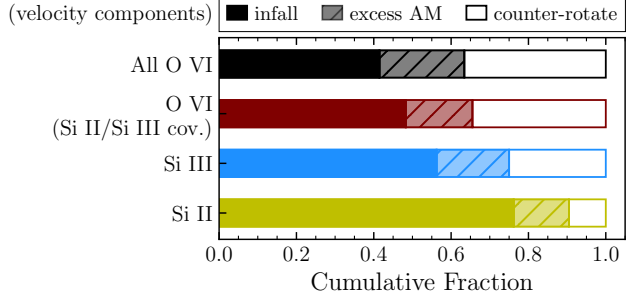


Figure 9. Comparison of angular momentum of Si II, Si III, and O VI velocity components with extended galaxy disk. Considering the hypothesis that non-counter-rotating velocity components trace gas on the extended disk plane, we compare the circular velocities of individual velocity components to that required for the gas to stay on circular orbits. Fraction of velocity components with lower (higher) velocities than needed are labeled as “infall” (“excess AM”) and are shown by the filled (light-colored hatched) histograms. Unfilled histograms represent counter-rotating velocity components. The fraction of infalling velocity components decreases with increasing ionization potential. This Figure follows the same color scheme as Figure 5.

and is infalling (filled histograms)¹³. The fraction of infalling velocity components clearly increases with decreasing ionization potential, for which only about 45% for O VI velocity components are tracing infalling gas, and this fraction increases to 80% for Si II. On the other hand, about 15% of the velocity components of each ion have excess angular momentum to be on the circular orbits (hatched). This gas is not expected to be accreting onto the disk.

With the infall interpretation, we can also determine the radii where the infalling gas joins the disk. Assuming the specific angular momentum of the gas remains unchanged, i.e., $R_{\text{ion}} V_{c,\text{ion}}$ stays constant, we calculate the radius where the gas has the same specific angular momentum as the extended disk (also known as the circularization radius). For Si II, Si III, and O VI gas, the calculation produces typical radii of under 50 kpc, which is comparable to the radii of extraplanar H I gas of nearby disk galaxies from 21-cm emission observations (e.g., Marasco et al. 2019).

The caveat of the above calculations is that while we assume the angular momentum is conserved for the gas clouds associated with individual velocity components, this may not be case according to cosmological simulations. Simulations have shown that the CGM has a

¹³ Velocity components that are consistent with being at the galaxy systemic velocities are considered as lacking sufficient angular momentum to stay on circular orbits.

broad angular momentum distribution (Stewart et al. 2013; DeFelippis et al. 2020; Hafen et al. 2022). This is due to the large turbulent velocity of the CGM, for which the turbulent motion adds a random angular momentum vector to the gas clouds (Fielding et al. 2017; Lochhaas et al. 2020; Pandya et al. 2023; Kakoly et al. 2025). However, this turbulent angular momentum component tends to cancel out when the gas accretes onto the galaxy disk (Hafen et al. 2022). In other words, the gas clouds often interact and exchange angular momentum with each other, implying that the angular momentum of a particular gas cloud is unlikely to be conserved during its infall to the disk.

Therefore, we repeat the analysis by comparing the circular velocities required for the gas to stay on circular orbits to the column-density-weighted velocities of different ions in individual sightlines. This enables us to consider the average angular momentum of the gas intersected along the sightlines instead of the gas clouds associated with individual velocity components. The result is shown in Figure 10. First of all, the fraction of counter-rotating O VI gas is only about 10%, which is four times lower than that calculated using individual velocity components ($\approx 40\%$). This reiterates the result from Figure 3 that net counter-rotating O VI absorbers are rare. Also, the infalling gas fractions of Si II, Si III, and O VI gas all reach $\approx 80\%$, which are higher than the calculations with individual velocity components, especially for O VI (45%). Because O VI traces gas out to larger 3D radii compared to the low ions, and the expected CGM rotation velocity decreases with increasing radius due to the net CGM angular momentum being roughly radius-independent (also see Section 4.1), the O VI corotation and/or infall signatures could be easily masked by the turbulent motion. Consequently, the corotation and/or infall of O VI gas is more likely to be observed only when we consider the average angular momentum using the column-density-weighted velocities in individual sightlines instead of individual velocity components.

4.3. Comparison with previous work on O VI kinematics and disk rotation

Unlike the numerous literatures that analyzed the relationship between low-ionization-state Mg II gas and disk rotation, very few work focused on this comparison with O VI (see Section 1). Using 10 major-axis sightlines with azimuthal angle below 25° , Kacprzak et al. (2019) showed that both the individual velocity components and weighted velocities per sightline of the O VI gas does not correlate with the disk rotation kinematics (their Figure 4). They also demonstrated that

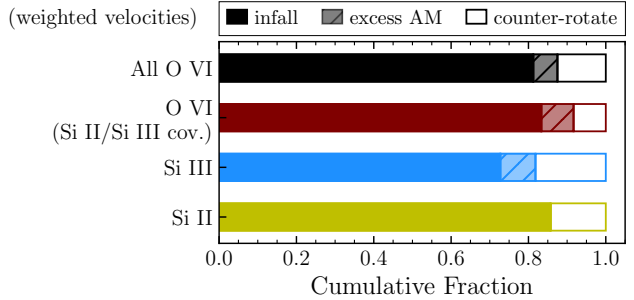


Figure 10. Comparison of angular momentum of the extended galaxy disk with the average Si II, Si III, and O VI gas in individual sightlines. Analogous to Figure 9, but instead of considering individual velocity components, this Figure shows the result using the column-density-weighted velocities of the gas detected in individual sightlines. Different ions show similar fractions of net counter-rotating gas and infalling gas. In particular, O VI has a lower counter-rotation fraction and a higher infall fraction compared to that from the calculation of using individual velocity components in Figure 9.

a simple monolithic rotating halo model failed to explain the full velocity spread of the O VI absorption. In contrast, when they ran AMR cosmological simulations, they clearly found infalling O VI filaments that rotate in the same direction as the galaxy disks. The inflowing O VI gas decelerates when it approaches the galaxies and becomes rotationally-dominated. However, the inflowing/rotating O VI signatures were washed out by other velocity structures in the CGM when they computed integrated velocities along lines of sight through the entire simulated galaxy halos. Therefore, inspired by their simulation analysis, they concluded that while corotating or accreting O VI gas could still exist in their observed sightlines, the signature was either weak or was masked by other kinematics ongoing within the CGM.

More recently, Kacprzak et al. (2025) conducted the COS-EDGES survey and analyzed the multiphase CGM of nine edge-on disk galaxies ($i \geq 60^\circ$) probed by major-axis sightlines at impact parameters below $\approx 0.3r_{\text{vir}}$. By comparing the stacked absorption-line profiles of different ions (e.g., Mg I, Mg II, and O VI) in the small ($\leq 0.2r_{\text{vir}}$) and large ($> 0.2r_{\text{vir}}$) impact parameter bins, they showed that while the Doppler sign of the weighted velocities are consistent with disk rotation, the velocity magnitude decreases with increasing impact parameters. More importantly, the amount of absorption that corotates with the disk declines with both increasing ionization potential and sightline impact parameters; in contrast to over 90% of the Mg II absorption that corotates with the disk, only 80% (60%) of the O VI absorption corotates at small (large) impact parameters. Hence,

they concluded that the CGM has a radially-dependent kinematic structure. Within $0.2r_{\text{vir}}$, the CGM hosts cool and dynamically broad gas that tightly coupled with disk rotation, whereas beyond $0.2r_{\text{vir}}$, especially for O VI, the CGM becomes less kinematically correlated with disk rotation due to the presence of corotating, lagging, and volume-filling components.

In general, our analysis agrees with both Kacprzak et al. (2019) and Kacprzak et al. (2025) that the corotation signature of O VI gas is challenging to observe due to kinematics components other than rotation. In particular, while individual O VI velocity components do not seem to correlate with disk rotation, the column-density-weighted velocities suggest that the bulk of O VI gas rarely counter-rotates (Figure 3). We have attributed this “discrepancy” to the turbulent motion of the CGM, and averaging is required to reveal the net O VI CGM angular momentum while searching for the corotation signature (Section 4.2). Furthermore, we have also compared the O VI kinematics to that of the low ions. Not only do low ions more often corotate with the disk compared to O VI (Figure 4), but the O VI velocity components with low-ion matches are more likely to corotate compared to those without low-ion matches (Figure 6). These results suggest that low ions are better indicators for identifying the corotating gas, which also matches the conclusion from Nateghi et al. (2024) and Kacprzak et al. (2025) that the lower the ionization potential, the more likely the ion is kinematically consistent with the rotation of the galaxy disks and supports the accretion scenario.

5. CONCLUSION

We presented a compilation of new and archival *HST/COS* observations of quasars behind $z \approx 0.2$, star-forming galaxies. All 18 quasar sightlines probe the CGM within 45° of the major axes of the host galaxies with inclined disks ($i \gtrsim 45^\circ$), doubling the existing number of major-axis sightlines in the literature for studying the relationship between the O VI and disk rotation kinematics.

We compared the kinematics of the O VI gas with that of the low-ionization-state gas (traced by Si II and Si III) and disk rotation. We showed that while individual velocity O VI components do not correlate with disk rotation, the bulk of O VI gas, as measured by the column-density-weighted O VI velocity in each sightline, rarely counter-rotates with the galaxy disk (Figure 3). In general, Si II and Si III gas are less likely to counter-rotate with the disk compared to O VI (Figures 4 and 5). But more importantly, we matched velocity components between O VI and low ions (Si II and Si III) by minimizing

the difference of their velocity centroids. We showed that the O VI velocity components with matches with low ions were mainly found in sightlines at small impact parameters of below 100 kpc, whereas those O VI velocity components without low-ion matches were on average at larger impact parameters. These low-ion-matched O VI velocity components are also more frequently corotate with the disk compared to those O VI velocity components without a low-ion match (Figure 7).

Previous literature has shown that low-ionization-state gas is commonly detected in the inner CGM, and major-axis sightlines often detect such gas to corotate with the galaxy disk. Although absorption-line measurements do not reveal where the gas lies along the line of sight, our results of the low-ion matched O VI velocity components sharing these properties suggest that these O VI components trace the gas that is co-spatial with that of the low ions, i.e., on the extended disk plane in the inner CGM. In contrast, the O VI velocity components without a low-ion match traces gas at large 3D radius. Furthermore, if some of the O VI gas resides on the extended disk plane, we asked the question that whether the gas has sufficient angular momentum to stay on circular orbits. If not, this could suggest the gas is infalling. We showed that about 45% of the O VI velocity components lack sufficient angular momentum to maintain a circular orbit. This fraction increases with decreasing ionization potential, with 80% of Si II velocity components tracing radially infalling gas (Figure 9). Interestingly, repeating this calculation using the column-density-weighted velocities increases the inflow fractions of O VI and Si III also to 80%. We interpret this result as a consequence of the turbulent motion adding random angular momentum vectors to the gas clouds associated with individual velocity components. Therefore, the corotation and inflow signatures are more likely to be observationally detected only when we consider the average angular momentum of the gas using the column-density-weighted velocities. Our future work will include photoionization modeling and geometric models for explaining the circumgalactic gas flows of O VI and low-ionization-state gas and to understand the CGM angular momentum and gas accretion onto galaxies.

This work was supported by NASA through HST-GO-15866.002-A from the Space Telescope Science Institute. We gratefully acknowledge the support for SHH from the National Science Foundation under AST-2202328. JS was supported by the Israel Science Foundation (grant No. 2584/21). Some observations reported here were obtained at the MMT Observatory, a joint facility of the

University of Arizona and the Smithsonian Institution. Some of the data presented herein were obtained at the W. M. Keck Observatory, which is operated as a scientific partnership among the California Institute of Technology, the University of California and the National Aeronautics and Space Administration. The Observatory was made possible by the generous financial support of the W. M. Keck Foundation. Some observations

were supported by Swinburne Keck programmes 2014B W018E, 2015 W187E, and 2016A W032E, W056E. Some presented data are based on observations obtained with the Apache Point Observatory 3.5 m telescope, which is owned and operated by the Astrophysical Research Consortium.

Facilities: HST (COS, ACS, WFPC2), MMT (Blue Channel spectrograph, Red Channel Spectrograph), Keck:I (LRIS), Keck:II (ESI, NIRC2), ARC

REFERENCES

- Behroozi, P. S., Conroy, C., & Wechsler, R. H. 2010, ApJ, 717, 379
- Blanton, M. R., Bershady, M. A., Abolfathi, B., et al. 2017, AJ, 154, 28
- Bordoloi, R., Lilly, S. J., Knobel, C., et al. 2011, ApJ, 743, 10
- Bouché, N., Hohensee, W., Vargas, R., et al. 2012, MNRAS, 426, 801
- Bryan, G. L., & Norman, M. L. 1998, ApJ, 495, 80
- Chabrier, G. 2003, PASP, 115, 763
- Chen, H.-W., Helsby, J. E., Gauthier, J.-R., et al. 2010, ApJ, 714, 1521
- Chen, H.-W., Zahedy, F. S., Boettcher, E., et al. 2020, MNRAS, 497, 498
- Churchill, C. W., Trujillo-Gomez, S., Nielsen, N. M., & Kacprzak, G. G. 2013, ApJ, 779, 87
- Davies, J. J., Crain, R. A., Oppenheimer, B. D., & Schaye, J. 2020, MNRAS, 491, 4462
- DeFelippis, D., Genel, S., Bryan, G. L., et al. 2020, ApJ, 895, 17
- Dutta, S., Muzahid, S., Schaye, J., et al. 2025, ApJ, 980, 264
- . 2024, arXiv e-prints, arXiv:2409.15423
- Faucher-Giguère, C.-A., & Oh, S. P. 2023, ARA&A, 61, 131
- Fielding, D., Quataert, E., McCourt, M., & Thompson, T. A. 2017, MNRAS, 466, 3810
- Geller, M. J., Hwang, H. S., Fabricant, D. G., et al. 2014, ApJS, 213, 35
- Hafen, Z., Stern, J., Bullock, J., et al. 2022, MNRAS, 514, 5056
- Hanuschik, R. W. 2003, A&A, 407, 1157
- Heckman, T., Borthakur, S., Wild, V., Schiminovich, D., & Bordoloi, R. 2017, ApJ, 846, 151
- Ho, S. H., & Martin, C. L. 2020, ApJ, 888, 14
- Ho, S. H., Martin, C. L., Kacprzak, G. G., & Churchill, C. W. 2017, ApJ, 835, 267
- Huang, Y.-H., Chen, H.-W., Shectman, S. A., et al. 2021, MNRAS, 502, 4743
- Hubble, E. P. 1926, ApJ, 64, 321
- Johnson, S. D., Chen, H.-W., & Mulchaey, J. S. 2013, MNRAS, 434, 1765
- . 2015, MNRAS, 449, 3263
- Johnson, S. D., Chen, H.-W., Mulchaey, J. S., Schaye, J., & Straka, L. A. 2017, ApJL, 850, L10
- Kacprzak, G. G., Churchill, C. W., Barton, E. J., & Cooke, J. 2011, ApJ, 733, 105
- Kacprzak, G. G., Churchill, C. W., Ceverino, D., et al. 2010, ApJ, 711, 533
- Kacprzak, G. G., Churchill, C. W., & Nielsen, N. M. 2012, ApJL, 760, L7
- Kacprzak, G. G., Muzahid, S., Churchill, C. W., Nielsen, N. M., & Charlton, J. C. 2015, ApJ, 815, 22
- Kacprzak, G. G., Vander Vliet, J. R., Nielsen, N. M., et al. 2019, ApJ, 870, 137
- Kacprzak, G. G., Oppenheimer, B. D., Nielsen, N. M., et al. 2025, PASA, submitted
- Kakoly, A., Stern, J., Faucher-Giguère, C.-A., et al. 2025, arXiv e-prints, arXiv:2504.17001
- Krogager, J.-K. 2018, arXiv e-prints, arXiv:1803.01187
- Kroupa, P. 2001, MNRAS, 322, 231
- Lochhaas, C., Bryan, G. L., Li, Y., Li, M., & Fielding, D. 2020, MNRAS, 493, 1461
- Madau, P., & Dickinson, M. 2014, ARA&A, 52, 415
- Marasco, A., Fraternali, F., Heald, G., et al. 2019, A&A, 631, A50
- Martin, C. L., Ho, S. H., Kacprzak, G. G., & Churchill, C. W. 2019, ApJ, 878, 84
- Mathews, W. G., & Prochaska, J. X. 2017, ApJL, 846, L24
- Mishra, N., Johnson, S. D., Rudie, G. C., et al. 2024, ApJ, 976, 149
- Morton, D. C. 2003, ApJS, 149, 205
- Nateghi, H., Kacprzak, G. G., Nielsen, N. M., et al. 2024, MNRAS, 534, 930
- Nelson, D., Kauffmann, G., Pillepich, A., et al. 2018, MNRAS, 477, 450

- Ng, M., Nielsen, N. M., Kacprzak, G. G., et al. 2019, ApJ, 886, 66
- Nielsen, N. M., Churchill, C. W., & Kacprzak, G. G. 2013, ApJ, 776, 115
- Nielsen, N. M., Kacprzak, G. G., Muzahid, S., et al. 2017, ApJ, 834, 148
- Nielsen, N. M., Kacprzak, G. G., Pointon, S. K., Churchill, C. W., & Murphy, M. T. 2018, ApJ, 869, 153
- Oke, J. B., Cohen, J. G., Carr, M., et al. 1995, PASP, 107, 375
- Oppenheimer, B. D., Crain, R. A., Schaye, J., et al. 2016, MNRAS, 460, 2157
- Pandya, V., Fielding, D. B., Bryan, G. L., et al. 2023, ApJ, 956, 118
- Planck Collaboration, Ade, P. A. R., Aghanim, N., et al. 2016, A&A, 594, A13
- Pointon, S. K., Nielsen, N. M., Kacprzak, G. G., et al. 2017, ApJ, 844, 23
- Qu, Z., Chen, H.-W., Johnson, S. D., et al. 2024, ApJ, 968, 8
- Rockosi, C., Stover, R., Kibrick, R., et al. 2010, in Society of Photo-Optical Instrumentation Engineers (SPIE) Conference Series, Vol. 7735, Society of Photo-Optical Instrumentation Engineers (SPIE) Conference Series, 0
- Salpeter, E. E. 1955, ApJ, 121, 161
- Sameer, Charlton, J. C., Wakker, B. P., et al. 2024, MNRAS, 530, 3827
- Schroetter, I., Bouché, N. F., Zabl, J., et al. 2019, MNRAS, 490, 4368
- Sheinis, A. I., Bolte, M., Epps, H. W., et al. 2002, PASP, 114, 851
- Steidel, C. C., Kollmeier, J. A., Shapley, A. E., et al. 2002, ApJ, 570, 526
- Stern, J., Faucher-Giguère, C.-A., Hennawi, J. F., et al. 2018, ApJ, 865, 91
- Stewart, K. R., Brooks, A. M., Bullock, J. S., et al. 2013, ApJ, 769, 74
- Sultan, I., Faucher-Giguère, C.-A., Stern, J., et al. 2025, MNRAS, 540, 1017
- Suresh, J., Rubin, K. H. R., Kannan, R., et al. 2017, MNRAS, 465, 2966
- Tchernyshyov, K., Werk, J. K., Wilde, M. C., et al. 2022, ApJ, 927, 147
- . 2023, ApJ, 949, 41
- Tody, D. 1986, in Society of Photo-Optical Instrumentation Engineers (SPIE) Conference Series, Vol. 627, Instrumentation in astronomy VI, ed. D. L. Crawford, 733
- Tody, D. 1993, in Astronomical Society of the Pacific Conference Series, Vol. 52, Astronomical Data Analysis Software and Systems II, ed. R. J. Hanisch, R. J. V. Brissenden, & J. Barnes, 173
- Tumlinson, J., Peeples, M. S., & Werk, J. K. 2017, ARA&A, 55, 389
- Tumlinson, J., Thom, C., Werk, J. K., et al. 2011, Science, 334, 948
- van Dokkum, P. G. 2001, PASP, 113, 1420
- Wenger, M., Ochsenbein, F., Egret, D., et al. 2000, A&AS, 143, 9
- Werk, J. K., Prochaska, J. X., Thom, C., et al. 2012, ApJS, 198, 3
- Werk, J. K., Prochaska, J. X., Cantalupo, S., et al. 2016, ApJ, 833, 54
- Wizinowich, P. L., Le Mignant, D., Bouchez, A. H., et al. 2006, PASP, 118, 297
- Zabl, J., Bouché, N. F., Schroetter, I., et al. 2019, MNRAS, 485, 1961

APPENDIX

A. ABSORPTION SYSTEM ASSOCIATED WITH INDIVIDUAL GALAXIES

This Appendix includes the Voigt profile fits of absorption associated with the target galaxies in individual sightlines. Figure 11 shows the Voigt profile fits,

and Table 6 lists the parameters of the fits. Because not all ions were used in the analysis of this paper, we only present the measurements in the Appendix.

Table 6. Results for Voigt Profile Fitting

Quasar	Galaxy	z_{gal}	ion	v (km s $^{-1}$)	b (km s $^{-1}$)	$\log N$ (log cm $^{-2}$)
J040148–054056	J040150–054047	0.21966	H I	-47.2 ± 3.2	25.8 ± 4.0	15.51 ± 0.08
J040148–054056	J040150–054047	0.21966	H I	-22.4 ± 3.7	50.7 ± 2.1	15.16 ± 0.11
J040148–054056	J040150–054047	0.21966	H I	-621.6 ± 3.4	17.1 ± 4.9	13.57 ± 0.07
J040148–054056	J040150–054047	0.21966	H I	-559.2 ± 1.5	21.2 ± 1.4	14.61 ± 0.04
J040148–054056	J040150–054047	0.21966	O VI	-40.6 ± 4.2	26.2 ± 6.2	14.26 ± 0.06
J040148–054056	J040150–054047	0.21966	O VI	23.6 ± 3.0	23.1 ± 4.3	14.31 ± 0.06
J040148–054056	J040150–054047	0.21966	C III	-52.4 ± 4.9	12.2 ± 7.7	13.80 ± 0.33
J040148–054056	J040150–054047	0.21966	C III	0.5 ± 4.9	22.4 ± 8.2	14.10 ± 0.28
J040148–054056	J040150–054047	0.21966	C III	-556.5 ± 11.8	29.2 ± 18.6	12.92 ± 0.18
J040148–054056	J040150–054047	0.21966	N III	-30.0 ± 8.1	9.6 ± 17.6	13.72 ± 0.36
J040148–054056	J040150–054047	0.21966	N III	23.1 ± 11.8	74.9 ± 11.2	14.55 ± 0.09
J040148–054056	J040150–054047	0.21966	Si III	-26.1 ± 6.1	32.5 ± 9.4	12.64 ± 0.08
J040148–054056	J040150–054047	0.21966	Si III	-606.1 ± 17.7	46.0 ± 27.1	12.35 ± 0.18
J040148–054056	J040150–054047	0.21966	Si IV	-43.5 ± 6.1	15.5 ± 9.3	12.94 ± 0.14
J040148–054056	J040150–054047	0.21966	S IV	-19.4 ± 3.9	29.3 ± 5.6	14.77 ± 0.07
J080704+360353	J080702+360141	0.088061	H I	-720.2 ± 3.0	31.9 ± 4.9	14.30 ± 0.12
J080704+360353	J080702+360141	0.088061	H I	-634.3 ± 12.9	7.3 ± 37.7	12.99 ± 0.26
J080704+360353	J080702+360141	0.088061	H I	-584.9 ± 7.2	10.8 ± 16.7	13.39 ± 0.23
J080704+360353	J080702+360141	0.088061	H I	-214.9 ± 3.3	33.0 ± 3.7	14.80 ± 0.15
J080704+360353	J080702+360141	0.088061	H I	-106.9 ± 3.3	23.0 ± 4.0	14.80 ± 0.24
J080704+360353	J080702+360141	0.088061	H I	-40.0 ± 4.7	5.0 ± 2.5	14.04 ± 0.74
J080704+360353	J080702+360141	0.088061	H I	105.3 ± 6.9	7.5 ± 22.6	13.20 ± 0.65
J080704+360353	J080702+360141	0.088061	H I	174.1 ± 4.7	17.9 ± 8.7	13.50 ± 0.10
J080704+360353	J080702+360141	0.088061	O VI	-115.4 ± 7.7	46.4 ± 11.4	14.43 ± 0.08
J080704+360353	J080702+360141	0.088061	O VI	107.7 ± 10.5	12.0 ± 17.5	14.12 ± 0.23
J080704+360353	J080702+360141	0.088061	O VI	175.2 ± 12.1	12.9 ± 21.6	13.99 ± 0.29
J080704+360353	J080702+360141	0.088061	C IV	-201.1 ± 9.4	24.9 ± 14.9	13.45 ± 0.21
J080704+360353	J080702+360141	0.088061	C IV	-105.5 ± 6.3	39.6 ± 9.3	14.07 ± 0.08
J080704+360353	J080702+360141	0.088061	C IV	145.5 ± 7.7	66.7 ± 10.5	14.21 ± 0.06
J080704+360353	J080702+360141	0.088061	N V	146.9 ± 12.1	63.8 ± 18.3	13.86 ± 0.11
J084349+261910	J084356+261855	0.11284	H I	-175.1 ± 10.8	11.4 ± 28.5	12.90 ± 0.23
J084349+261910	J084356+261855	0.11284	H I	92.7 ± 2.4	45.4 ± 3.3	14.50 ± 0.06
J084349+261910	J084356+261855	0.11284	H I	254.0 ± 9.4	42.6 ± 12.5	13.42 ± 0.11
J084349+261910	J084356+261855	0.11284	O VI	-188.3 ± 15.1	30.6 ± 22.7	13.70 ± 0.19
J084349+261910	J084356+261855	0.11284	O VI	80.5 ± 8.9	70.3 ± 12.7	14.37 ± 0.05
J084349+261910	J084356+261855	0.11284	Si III	-156.8 ± 9.7	21.5 ± 20.3	12.40 ± 0.18
J084349+261910	J084356+261855	0.11284	Si III	87.6 ± 8.4	10.3 ± 29.0	12.44 ± 0.65
J084349+261910	J084356+261855	0.11284	Si II	-152.5 ± 7.8	13.0 ± 19.1	12.86 ± 0.16
J085215+171143	J085215+171137	0.16921	H I	-807.7 ± 3.3	36.2 ± 4.8	13.74 ± 0.04
J085215+171143	J085215+171137	0.16921	H I	-600.5 ± 8.5	34.4 ± 13.0	13.23 ± 0.11

Table 6 *continued*

Table 6 (*continued*)

Quasar	Galaxy	z_{gal}	ion	v (km s $^{-1}$)	b (km s $^{-1}$)	$\log N$ (log cm $^{-2}$)
J085215+171143	J085215+171137	0.16921	H I	-57.7 ± 1.5	41.5 ± 0.6	18.72 ± 0.05
J085215+171143	J085215+171137	0.16921	H I	91.0 ± 42.8	69.1 ± 11.0	13.74 ± 0.37
J085215+171143	J085215+171137	0.16921	C II	-899.7 ± 4.6	18.9 ± 8.4	13.77 ± 0.09
J085215+171143	J085215+171137	0.16921	C II	-832.5 ± 2.3	23.2 ± 4.1	14.24 ± 0.04
J085215+171143	J085215+171137	0.16921	O VI	-882.8 ± 4.1	4.1 ± 9.7	13.54 ± 0.23
J085215+171143	J085215+171137	0.16921	O VI	-800.8 ± 2.6	6.8 ± 5.2	13.94 ± 0.21
J085215+171143	J085215+171137	0.16921	O VI	-607.9 ± 8.5	45.6 ± 13.2	13.85 ± 0.09
J085215+171143	J085215+171137	0.16921	O VI	-39.5 ± 9.2	64.9 ± 15.5	14.64 ± 0.07
J085215+171143	J085215+171137	0.16921	C III	-808.7 ± 17.7	40.9 ± 31.1	12.92 ± 0.20
J085215+171143	J085215+171137	0.16921	C III	-246.7 ± 10.3	8.5 ± 21.9	12.68 ± 0.23
J085215+171143	J085215+171137	0.16921	C III	-70.8 ± 6.2	59.5 ± 10.8	15.11 ± 0.34
J085215+171143	J085215+171137	0.16921	C III	50.5 ± 6.9	11.1 ± 13.1	13.55 ± 0.48
J085215+171143	J085215+171137	0.16921	N II	-802.3 ± 15.4	39.8 ± 25.5	13.58 ± 0.18
J085215+171143	J085215+171137	0.16921	N II	-224.6 ± 8.5	4.9 ± 27.5	13.25 ± 0.54
J085215+171143	J085215+171137	0.16921	N II	-133.3 ± 7.7	16.6 ± 11.9	13.77 ± 0.21
J085215+171143	J085215+171137	0.16921	N II	-47.7 ± 9.7	43.9 ± 13.4	14.83 ± 0.10
J085215+171143	J085215+171137	0.16921	N II	6.9 ± 5.1	11.8 ± 11.8	14.51 ± 0.55
J085215+171143	J085215+171137	0.16921	N II	70.3 ± 7.7	19.5 ± 13.6	13.65 ± 0.15
J085215+171143	J085215+171137	0.16921	N III	-121.0 ± 13.3	34.5 ± 12.8	14.48 ± 0.19
J085215+171143	J085215+171137	0.16921	N III	-42.1 ± 12.8	34.1 ± 22.7	14.97 ± 0.18
J085215+171143	J085215+171137	0.16921	N III	15.1 ± 10.0	16.0 ± 12.4	14.90 ± 0.97
J085215+171143	J085215+171137	0.16921	O I	-835.9 ± 3.6	9.6 ± 7.8	14.44 ± 0.23
J085215+171143	J085215+171137	0.16921	O I	-645.9 ± 6.9	24.5 ± 12.6	14.25 ± 0.10
J085215+171143	J085215+171137	0.16921	O I	-220.5 ± 9.2	26.6 ± 17.1	14.13 ± 0.12
J085215+171143	J085215+171137	0.16921	O I	-62.6 ± 4.1	34.6 ± 6.3	14.88 ± 0.05
J085215+171143	J085215+171137	0.16921	O I	7.2 ± 4.9	6.2 ± 11.1	14.30 ± 0.74
J085215+171143	J085215+171137	0.16921	O I	79.7 ± 6.7	2.6 ± 2.3	14.40 ± 0.68
J085215+171143	J085215+171137	0.16921	S III	-221.5 ± 4.4	17.4 ± 7.4	14.25 ± 0.08
J085215+171143	J085215+171137	0.16921	S III	-68.2 ± 6.7	38.6 ± 10.3	14.49 ± 0.08
J085215+171143	J085215+171137	0.16921	S III	-2.8 ± 3.6	9.2 ± 7.4	14.41 ± 0.17
J085215+171143	J085215+171137	0.16921	Si II	-264.9 ± 7.9	15.8 ± 14.6	12.76 ± 0.17
J085215+171143	J085215+171137	0.16921	Si II	-64.1 ± 12.3	50.4 ± 9.2	14.16 ± 0.12
J085215+171143	J085215+171137	0.16921	Si II	-5.1 ± 5.1	22.7 ± 6.1	14.00 ± 0.16
J085215+171143	J085215+171137	0.16921	Si III	-188.2 ± 36.4	40.4 ± 27.3	13.09 ± 0.50
J085215+171143	J085215+171137	0.16921	Si III	-76.7 ± 9.0	52.2 ± 37.1	14.17 ± 0.34
J085215+171143	J085215+171137	0.16921	Si III	17.7 ± 8.2	18.1 ± 14.0	13.77 ± 0.72
J085215+171143	J085215+171137	0.16921	Si III	76.9 ± 7.4	15.6 ± 13.7	12.55 ± 0.18
J085215+171143	J085215+171137	0.16921	Fe II	-58.2 ± 5.9	31.8 ± 9.8	14.15 ± 0.08
J085215+171143	J085215+171137	0.16921	Fe II	5.6 ± 3.8	8.0 ± 9.2	13.97 ± 0.25
J085215+171143	J085215+171137	0.16921	Fe III	-44.4 ± 12.1	47.2 ± 15.5	14.70 ± 0.12
J085215+171143	J085215+171137	0.16921	Fe III	12.8 ± 6.9	12.1 ± 17.9	14.08 ± 0.45
J091954+291408	J091954+291345	0.23288	H I	-283.5 ± 5.6	2.5 ± 1.7	14.57 ± 0.59
J091954+291408	J091954+291345	0.23288	H I	-150.0 ± 3.2	31.6 ± 3.1	19.14 ± 0.59
J091954+291408	J091954+291345	0.23288	H I	-19.0 ± 3.6	22.6 ± 3.9	16.76 ± 0.21
J091954+291408	J091954+291345	0.23288	H I	149.1 ± 1.7	37.6 ± 3.9	18.82 ± 0.60
J091954+291408	J091954+291345	0.23288	C II	-157.6 ± 8.3	37.9 ± 12.7	14.21 ± 0.10
J091954+291408	J091954+291345	0.23288	C II	122.8 ± 46.7	51.1 ± 32.8	14.64 ± 0.47
J091954+291408	J091954+291345	0.23288	C II	173.6 ± 17.3	19.0 ± 26.0	14.73 ± 0.73
J091954+291408	J091954+291345	0.23288	O VI	-209.4 ± 4.9	16.2 ± 8.9	14.21 ± 0.19
J091954+291408	J091954+291345	0.23288	O VI	-110.9 ± 5.1	12.0 ± 9.0	14.04 ± 0.19
J091954+291408	J091954+291345	0.23288	O VI	-38.4 ± 11.7	28.8 ± 20.7	13.85 ± 0.17
J091954+291408	J091954+291345	0.23288	O VI	46.9 ± 11.4	7.3 ± 22.0	13.61 ± 0.23
J091954+291408	J091954+291345	0.23288	O VI	100.9 ± 16.3	16.1 ± 37.8	13.58 ± 0.41

Table 6 *continued*

Table 6 (*continued*)

Quasar	Galaxy	z_{gal}	ion	v (km s $^{-1}$)	b (km s $^{-1}$)	$\log N$ (log cm $^{-2}$)
J091954+291408	J091954+291345	0.23288	O VI	162.9 \pm 9.7	15.2 \pm 16.7	13.93 \pm 0.16
J091954+291408	J091954+291345	0.23288	C III	-167.3 \pm 27.2	53.4 \pm 21.4	14.00 \pm 0.24
J091954+291408	J091954+291345	0.23288	C III	-105.5 \pm 10.7	19.1 \pm 19.5	14.01 \pm 0.74
J091954+291408	J091954+291345	0.23288	C III	-18.0 \pm 5.8	29.3 \pm 11.1	13.61 \pm 0.09
J091954+291408	J091954+291345	0.23288	C III	45.0 \pm 8.8	8.4 \pm 18.7	13.26 \pm 0.32
J091954+291408	J091954+291345	0.23288	C III	151.7 \pm 6.8	50.4 \pm 15.0	14.73 \pm 0.45
J091954+291408	J091954+291345	0.23288	N II	94.6 \pm 5.8	13.4 \pm 11.2	14.08 \pm 0.15
J091954+291408	J091954+291345	0.23288	N II	168.5 \pm 5.1	27.2 \pm 9.2	14.33 \pm 0.09
J094331+053131	J094330+053118	0.353052	H I	36.3 \pm 2.9	43.7 \pm 2.9	14.78 \pm 0.04
J094331+053131	J094330+053118	0.353052	H I	245.5 \pm 9.5	43.9 \pm 6.2	15.16 \pm 0.09
J094331+053131	J094330+053118	0.353052	H I	334.3 \pm 1.8	26.9 \pm 2.5	16.12 \pm 0.04
J094331+053131	J094330+053118	0.353052	H I	413.0 \pm 2.2	25.7 \pm 2.9	15.88 \pm 0.04
J094331+053131	J094330+053118	0.353052	H I	483.2 \pm 19.9	74.7 \pm 13.4	14.98 \pm 0.13
J094331+053131	J094330+053118	0.353052	H I	672.7 \pm 6.6	17.2 \pm 10.5	13.42 \pm 0.16
J094331+053131	J094330+053118	0.353052	H I	816.0 \pm 4.2	6.1 \pm 5.0	13.51 \pm 0.38
J094331+053131	J094330+053118	0.353052	H I	940.6 \pm 6.0	19.9 \pm 10.9	13.06 \pm 0.31
J094331+053131	J094330+053118	0.353052	O VI	49.6 \pm 1.8	20.1 \pm 2.6	14.64 \pm 0.08
J094331+053131	J094330+053118	0.353052	O VI	161.1 \pm 4.4	11.0 \pm 10.0	13.32 \pm 0.31
J094331+053131	J094330+053118	0.353052	O VI	397.9 \pm 4.4	13.6 \pm 7.0	13.75 \pm 0.12
J094331+053131	J094330+053118	0.353052	C III	37.4 \pm 2.2	9.1 \pm 4.5	13.36 \pm 0.25
J094331+053131	J094330+053118	0.353052	C III	195.0 \pm 1.8	24.1 \pm 6.9	14.72 \pm 0.67
J094331+053131	J094330+053118	0.353052	C III	274.1 \pm 7.3	10.8 \pm 13.2	12.70 \pm 0.22
J094331+053131	J094330+053118	0.353052	C III	329.5 \pm 2.7	15.0 \pm 4.1	13.42 \pm 0.10
J094331+053131	J094330+053118	0.353052	C III	407.9 \pm 2.0	11.6 \pm 4.2	13.55 \pm 0.24
J094331+053131	J094330+053118	0.353052	C III	531.1 \pm 4.9	19.9 \pm 7.5	13.12 \pm 0.10
J094331+053131	J094330+053118	0.353052	C III	667.4 \pm 5.3	12.5 \pm 8.6	12.88 \pm 0.15
J094331+053131	J094330+053118	0.353052	C III	808.5 \pm 6.0	4.0 \pm 18.7	12.58 \pm 0.61
J094331+053131	J094330+053118	0.353052	C III	923.5 \pm 5.1	2.6 \pm 11.7	12.65 \pm 0.31
J094331+053131	J094330+053118	0.353052	N V	43.2 \pm 3.8	13.0 \pm 6.0	13.90 \pm 0.16
J094331+053131	J094330+053118	0.353052	N V	129.6 \pm 4.7	14.3 \pm 7.9	13.37 \pm 0.20
J094331+053131	J094330+053118	0.353052	N V	383.8 \pm 4.7	9.6 \pm 8.2	13.71 \pm 0.18
J094331+053131	J094330+053118	0.353052	Si III	411.2 \pm 5.5	11.3 \pm 9.6	12.51 \pm 0.24
J103640+565125	J103643+565119	0.13629	H I	-38.5 \pm 2.9	17.6 \pm 3.4	14.35 \pm 0.11
J103640+565125	J103643+565119	0.13629	H I	18.2 \pm 5.3	19.7 \pm 8.1	13.57 \pm 0.10
J103640+565125	J103643+565119	0.13629	Si III	-56.7 \pm 14.0	29.7 \pm 23.0	12.64 \pm 0.20
J103640+565125	J103643+565119	0.13629	Si III	29.0 \pm 4.7	16.6 \pm 7.9	12.86 \pm 0.14
J104116+061016	J104117+061018	0.442173	H I	-160.5 \pm 5.8	38.3 \pm 4.0	16.66 \pm 0.29
J104116+061016	J104117+061018	0.442173	H I	-67.8 \pm 9.6	30.1 \pm 4.8	15.21 \pm 0.17
J104116+061016	J104117+061018	0.442173	H I	63.4 \pm 16.2	54.0 \pm 31.9	13.27 \pm 0.18
J104116+061016	J104117+061018	0.442173	H I	173.6 \pm 4.2	9.5 \pm 9.2	13.33 \pm 0.28
J104116+061016	J104117+061018	0.442173	H I	199.6 \pm 10.4	40.9 \pm 8.4	13.70 \pm 0.13
J104116+061016	J104117+061018	0.442173	C II	-207.7 \pm 4.8	17.7 \pm 5.4	14.11 \pm 0.12
J104116+061016	J104117+061018	0.442173	C II	-152.8 \pm 2.5	21.5 \pm 4.6	14.75 \pm 0.13
J104116+061016	J104117+061018	0.442173	C II	-80.4 \pm 2.5	19.2 \pm 4.2	14.18 \pm 0.06
J104116+061016	J104117+061018	0.442173	C II	57.2 \pm 4.4	21.9 \pm 6.5	13.91 \pm 0.08
J104116+061016	J104117+061018	0.442173	O VI	-182.7 \pm 5.0	15.8 \pm 7.7	13.82 \pm 0.16
J104116+061016	J104117+061018	0.442173	O VI	-123.9 \pm 4.8	30.9 \pm 10.7	14.28 \pm 0.09
J104116+061016	J104117+061018	0.442173	O VI	-49.9 \pm 7.5	30.2 \pm 9.8	14.06 \pm 0.12
J104116+061016	J104117+061018	0.442173	C III	-135.3 \pm 1.2	45.6 \pm 3.7	14.96 \pm 0.17
J104116+061016	J104117+061018	0.442173	C III	93.5 \pm 1.5	30.4 \pm 2.2	13.82 \pm 0.03
J104116+061016	J104117+061018	0.442173	N II	-151.3 \pm 4.4	23.1 \pm 6.3	14.43 \pm 0.11
J104116+061016	J104117+061018	0.442173	N III	-140.3 \pm 2.1	41.1 \pm 3.5	14.58 \pm 0.02
J104116+061016	J104117+061018	0.442173	N III	-63.6 \pm 2.1	7.2 \pm 4.3	13.93 \pm 0.14

Table 6 *continued*

Table 6 (*continued*)

Quasar	Galaxy	z_{gal}	ion	v (km s $^{-1}$)	b (km s $^{-1}$)	$\log N$ (log cm $^{-2}$)
J104116+061016	J104117+061018	0.442173	Si II	-187.3 ± 22.0	19.1 ± 25.3	12.87 ± 0.47
J104116+061016	J104117+061018	0.442173	Si II	-149.9 ± 3.1	11.7 ± 4.6	13.72 ± 0.22
J104116+061016	J104117+061018	0.442173	Si II	-64.6 ± 8.5	32.7 ± 13.7	13.02 ± 0.12
J104116+061016	J104117+061018	0.442173	Si II	11.8 ± 5.2	13.6 ± 8.7	12.84 ± 0.15
J104116+061016	J104117+061018	0.442173	Si II	209.7 ± 5.2	18.0 ± 8.2	12.90 ± 0.12
J104116+061016	J104117+061018	0.442173	Si III	-199.8 ± 8.3	12.2 ± 8.7	12.70 ± 0.28
J104116+061016	J104117+061018	0.442173	Si III	-155.5 ± 5.0	18.5 ± 13.2	13.65 ± 0.34
J104116+061016	J104117+061018	0.442173	Si III	-98.9 ± 14.1	50.6 ± 11.6	13.54 ± 0.14
J104116+061016	J104117+061018	0.442173	Si III	57.4 ± 7.5	43.4 ± 11.3	12.76 ± 0.08
J113910-135043	J113911-135108	0.204194	H I	-414.3 ± 3.5	7.7 ± 7.0	13.04 ± 0.17
J113910-135043	J113911-135108	0.204194	H I	-319.7 ± 7.0	18.3 ± 11.3	13.04 ± 0.16
J113910-135043	J113911-135108	0.204194	H I	-271.9 ± 2.5	3.0 ± 1.4	13.94 ± 0.29
J113910-135043	J113911-135108	0.204194	H I	-248.0 ± 3.0	7.1 ± 5.3	13.50 ± 0.30
J113910-135043	J113911-135108	0.204194	H I	-20.7 ± 4.5	23.9 ± 3.1	16.27 ± 0.30
J113910-135043	J113911-135108	0.204194	H I	41.1 ± 13.9	25.6 ± 16.1	15.11 ± 0.27
J113910-135043	J113911-135108	0.204194	H I	95.4 ± 8.2	22.8 ± 14.1	14.25 ± 0.46
J113910-135043	J113911-135108	0.204194	H I	151.1 ± 2.0	14.0 ± 3.5	16.15 ± 0.30
J113910-135043	J113911-135108	0.204194	H I	193.7 ± 5.5	17.5 ± 3.6	14.58 ± 0.16
J113910-135043	J113911-135108	0.204194	C II	-18.2 ± 10.7	27.3 ± 16.9	13.76 ± 0.17
J113910-135043	J113911-135108	0.204194	C II	55.3 ± 17.7	23.7 ± 33.0	13.19 ± 0.49
J113910-135043	J113911-135108	0.204194	O VI	-227.0 ± 8.7	10.5 ± 19.8	13.26 ± 0.32
J113910-135043	J113911-135108	0.204194	O VI	-13.2 ± 14.9	36.7 ± 18.6	14.14 ± 0.20
J113910-135043	J113911-135108	0.204194	O VI	61.0 ± 11.9	40.7 ± 29.7	14.12 ± 0.29
J113910-135043	J113911-135108	0.204194	C III	-391.4 ± 4.2	5.0 ± 10.5	12.80 ± 0.34
J113910-135043	J113911-135108	0.204194	C III	-8.5 ± 6.5	31.9 ± 6.2	14.32 ± 0.16
J113910-135043	J113911-135108	0.204194	C III	45.8 ± 6.0	10.9 ± 13.8	13.58 ± 0.31
J113910-135043	J113911-135108	0.204194	C III	80.7 ± 6.0	15.2 ± 6.9	13.46 ± 0.13
J113910-135043	J113911-135108	0.204194	C III	156.1 ± 2.7	5.8 ± 6.8	13.09 ± 0.47
J113910-135043	J113911-135108	0.204194	N III	-9.7 ± 7.0	31.7 ± 10.2	13.98 ± 0.10
J113910-135043	J113911-135108	0.204194	N III	73.9 ± 13.2	35.8 ± 19.5	13.76 ± 0.17
J113910-135043	J113911-135108	0.204194	Si III	-435.2 ± 9.0	35.1 ± 13.2	12.71 ± 0.11
J113910-135043	J113911-135108	0.204194	Si III	-233.0 ± 16.7	67.9 ± 24.0	12.72 ± 0.14
J113910-135043	J113911-135108	0.204194	Si III	-5.7 ± 2.7	27.5 ± 4.5	13.46 ± 0.07
J113910-135043	J113911-135108	0.204194	Si III	46.3 ± 2.7	6.6 ± 6.8	12.89 ± 0.49
J113910-135043	J113911-135108	0.204194	Si III	83.7 ± 3.0	13.4 ± 4.9	12.85 ± 0.10
J113910-135043	J113911-135108	0.204194	Si III	158.3 ± 3.2	10.1 ± 5.4	12.63 ± 0.12
J113910-135043	J113909-135053	0.319255	H I	-602.0 ± 0.7	16.7 ± 1.0	15.38 ± 0.10
J113910-135043	J113909-135053	0.319255	H I	-101.4 ± 0.9	30.8 ± 1.2	14.91 ± 0.02
J113910-135043	J113909-135053	0.319255	H I	48.4 ± 0.5	23.4 ± 0.3	16.14 ± 0.02
J113910-135043	J113909-135053	0.319255	O VI	-83.9 ± 4.3	59.8 ± 6.9	14.11 ± 0.04
J113910-135043	J113909-135053	0.319255	O VI	37.7 ± 2.0	29.4 ± 3.4	14.01 ± 0.04
J113910-135043	J113909-135053	0.319255	O VI	159.8 ± 6.6	14.3 ± 10.8	13.45 ± 0.16
J113910-135043	J113909-135053	0.319255	C III	-601.3 ± 2.5	11.8 ± 4.5	13.16 ± 0.10
J113910-135043	J113909-135053	0.319255	C III	-113.8 ± 1.8	19.1 ± 2.8	13.53 ± 0.04
J113910-135043	J113909-135053	0.319255	C III	-73.2 ± 2.5	9.0 ± 5.1	12.94 ± 0.11
J113910-135043	J113909-135053	0.319255	C III	17.0 ± 14.3	33.1 ± 9.2	13.06 ± 0.24
J113910-135043	J113909-135053	0.319255	C III	43.4 ± 1.8	14.2 ± 4.0	13.58 ± 0.11
J123335+475800	J123338+475757	0.22171	H I	-61.1 ± 4.7	14.6 ± 3.9	14.14 ± 0.12
J123335+475800	J123338+475757	0.22171	H I	-2.7 ± 13.5	15.1 ± 12.8	15.17 ± 0.60
J123335+475800	J123338+475757	0.22171	H I	69.7 ± 14.5	43.7 ± 8.0	16.50 ± 0.30
J123335+475800	J123338+475757	0.22171	H I	96.2 ± 24.0	25.7 ± 17.4	16.16 ± 0.78
J123335+475800	J123338+475757	0.22171	C II	-1.2 ± 2.7	16.0 ± 4.5	13.79 ± 0.07
J123335+475800	J123338+475757	0.22171	C II	59.4 ± 1.2	17.0 ± 2.2	14.42 ± 0.07

Table 6 *continued*

Table 6 (*continued*)

Quasar	Galaxy	z_{gal}	ion	v (km s $^{-1}$)	b (km s $^{-1}$)	$\log N$ (log cm $^{-2}$)
J123335+475800	J123338+475757	0.22171	C II	119.5 \pm 2.7	7.2 \pm 6.2	13.49 \pm 0.13
J123335+475800	J123338+475757	0.22171	O VI	60.9 \pm 11.0	112.2 \pm 15.3	14.59 \pm 0.05
J123335+475800	J123338+475757	0.22171	C III	-66.7 \pm 1.5	9.5 \pm 4.4	14.02 \pm 0.61
J123335+475800	J123338+475757	0.22171	C III	-7.9 \pm 3.2	19.5 \pm 5.2	13.88 \pm 0.13
J123335+475800	J123338+475757	0.22171	C III	84.4 \pm 3.4	37.7 \pm 7.2	14.64 \pm 0.28
J123335+475800	J123338+475757	0.22171	N II	-9.3 \pm 10.1	31.3 \pm 16.7	13.65 \pm 0.16
J123335+475800	J123338+475757	0.22171	N II	56.2 \pm 2.2	14.1 \pm 3.7	14.09 \pm 0.07
J123335+475800	J123338+475757	0.22171	N III	9.1 \pm 18.9	89.8 \pm 18.3	14.35 \pm 0.11
J123335+475800	J123338+475757	0.22171	N III	66.0 \pm 3.4	14.1 \pm 6.6	14.18 \pm 0.13
J123335+475800	J123338+475757	0.22171	Si II	-1.7 \pm 3.4	12.4 \pm 6.2	12.67 \pm 0.10
J123335+475800	J123338+475757	0.22171	Si II	59.4 \pm 2.5	22.8 \pm 3.5	13.25 \pm 0.05
J123335+475800	J123338+475757	0.22171	Si III	-16.9 \pm 15.9	42.0 \pm 22.6	12.54 \pm 0.21
J123335+475800	J123338+475757	0.22171	Si III	62.1 \pm 2.7	15.0 \pm 8.2	13.42 \pm 0.24
J123335+475800	J123338+475757	0.22171	Si III	101.6 \pm 28.0	43.9 \pm 21.2	13.11 \pm 0.31
J123335+475800	J123338+475757	0.22171	Si IV	54.0 \pm 2.0	10.3 \pm 3.1	13.28 \pm 0.10
J132222+464546	J132222+464546	0.214431	H I	-20.2 \pm 6.9	36.9 \pm 2.6	16.52 \pm 0.12
J132222+464546	J132222+464546	0.214431	H I	56.0 \pm 5.9	31.8 \pm 2.2	16.91 \pm 0.14
J132222+464546	J132222+464546	0.214431	C II	-32.3 \pm 3.5	23.4 \pm 5.2	14.08 \pm 0.06
J132222+464546	J132222+464546	0.214431	C II	49.9 \pm 3.5	28.1 \pm 5.5	14.14 \pm 0.06
J132222+464546	J132222+464546	0.214431	O VI	-54.1 \pm 6.2	36.8 \pm 7.1	14.39 \pm 0.10
J132222+464546	J132222+464546	0.214431	O VI	37.3 \pm 22.0	64.8 \pm 22.4	14.19 \pm 0.17
J132222+464546	J132222+464546	0.214431	C III	-38.0 \pm 7.4	44.5 \pm 7.3	14.26 \pm 0.09
J132222+464546	J132222+464546	0.214431	C III	53.8 \pm 7.7	36.1 \pm 7.5	14.07 \pm 0.10
J132222+464546	J132222+464546	0.214431	N II	52.1 \pm 5.4	11.5 \pm 9.6	13.64 \pm 0.13
J132222+464546	J132222+464546	0.214431	N III	-37.0 \pm 11.1	36.6 \pm 17.4	14.04 \pm 0.12
J132222+464546	J132222+464546	0.214431	N III	54.6 \pm 7.9	33.1 \pm 11.9	14.10 \pm 0.12
J132222+464546	J132222+464546	0.214431	N V	-53.1 \pm 4.7	20.2 \pm 7.6	13.60 \pm 0.12
J132222+464546	J132222+464546	0.214431	Si II	-21.5 \pm 4.4	37.1 \pm 6.5	13.14 \pm 0.06
J132222+464546	J132222+464546	0.214431	Si II	61.7 \pm 3.7	9.4 \pm 6.3	12.86 \pm 0.11
J132222+464546	J132222+464546	0.214431	Si II	101.5 \pm 6.9	10.4 \pm 12.6	12.38 \pm 0.20
J132222+464546	J132222+464546	0.214431	Si II	161.7 \pm 4.0	8.4 \pm 7.2	12.59 \pm 0.16
J132222+464546	J132222+464546	0.214431	Si III	-92.8 \pm 6.2	15.6 \pm 10.7	12.46 \pm 0.15
J132222+464546	J132222+464546	0.214431	Si III	-21.0 \pm 2.2	27.3 \pm 4.2	13.42 \pm 0.06
J132222+464546	J132222+464546	0.214431	Si III	56.3 \pm 2.5	16.9 \pm 4.8	13.41 \pm 0.14
J132222+464546	J132222+464546	0.214431	Si III	105.2 \pm 10.1	12.5 \pm 17.6	12.40 \pm 0.27
J132222+464546	J132222+464546	0.214431	Si III	166.1 \pm 5.9	18.1 \pm 10.0	12.46 \pm 0.14
J132222+464546	J132222+464546	0.214431	Si IV	-38.5 \pm 6.4	26.9 \pm 9.4	13.04 \pm 0.11
J132222+464546	J132222+464546	0.214431	Si IV	52.1 \pm 7.2	13.2 \pm 11.4	12.89 \pm 0.17
J135522+303324	J135521+303320	0.20690	H I	-126.2 \pm 5.2	8.0 \pm 11.7	13.80 \pm 0.17
J135522+303324	J135521+303320	0.20690	H I	-23.1 \pm 1.2	25.1 \pm 2.3	16.21 \pm 0.27
J135522+303324	J135521+303320	0.20690	C II	-29.8 \pm 16.6	64.4 \pm 25.4	13.82 \pm 0.12
J135522+303324	J135521+303320	0.20690	O VI	-120.5 \pm 28.6	90.8 \pm 44.6	13.86 \pm 0.21
J135522+303324	J135521+303320	0.20690	O VI	7.0 \pm 4.0	38.7 \pm 5.6	14.36 \pm 0.05
J135522+303324	J135521+303320	0.20690	C III	-18.6 \pm 2.2	24.8 \pm 7.3	14.42 \pm 0.52
J135522+303324	J135521+303320	0.20690	N III	1.0 \pm 7.5	39.4 \pm 12.4	13.96 \pm 0.10
J135522+303324	J135521+303320	0.20690	N III	89.2 \pm 6.7	10.3 \pm 19.3	13.51 \pm 0.49
J142501+382100	J142459+382113	0.21295	H I	-518.5 \pm 1.7	28.9 \pm 2.0	15.35 \pm 0.05
J142501+382100	J142459+382113	0.21295	H I	-28.4 \pm 1.7	13.1 \pm 2.8	16.53 \pm 0.64
J142501+382100	J142459+382113	0.21295	H I	48.7 \pm 1.7	23.1 \pm 2.0	15.78 \pm 0.11
J142501+382100	J142459+382113	0.21295	O VI	-27.7 \pm 5.9	7.3 \pm 13.0	13.62 \pm 0.34
J142501+382100	J142459+382113	0.21295	O VI	32.4 \pm 4.7	27.9 \pm 8.2	14.18 \pm 0.07
J142501+382100	J142459+382113	0.21295	C III	-22.7 \pm 3.2	11.1 \pm 9.6	14.12 \pm 0.84
J142501+382100	J142459+382113	0.21295	C III	43.7 \pm 4.4	27.8 \pm 6.9	13.72 \pm 0.07

Table 6 *continued*

Table 6 (*continued*)

Quasar	Galaxy	z_{gal}	ion	v (km s $^{-1}$)	b (km s $^{-1}$)	$\log N$ (log cm $^{-2}$)
J142501+382100	J142459+382113	0.21295	N II	53.1 ± 10.6	26.4 ± 19.5	13.81 ± 0.21
J154741+343357	J154741+343350	0.18392	H I	-50.6 ± 15.4	46.7 ± 21.4	16.11 ± 0.66
J154741+343357	J154741+343350	0.18392	H I	59.8 ± 12.4	11.4 ± 4.2	19.34 ± 0.88
J154741+343357	J154741+343350	0.18392	O VI	-145.3 ± 4.8	33.3 ± 7.5	14.47 ± 0.07
J154741+343357	J154741+343350	0.18392	O VI	-11.4 ± 9.4	49.5 ± 13.6	14.68 ± 0.09
J154741+343357	J154741+343350	0.18392	O VI	70.1 ± 5.1	18.3 ± 9.7	14.99 ± 0.23
J154741+343357	J154741+343350	0.18392	O VI	125.3 ± 16.0	20.8 ± 25.9	13.71 ± 0.38
J154741+343357	J154741+343350	0.18392	C II	-30.4 ± 3.0	35.5 ± 10.8	15.54 ± 0.67
J154741+343357	J154741+343350	0.18392	C II	83.6 ± 7.6	4.5 ± 19.3	13.76 ± 0.53
J154741+343357	J154741+343350	0.18392	C III	-195.0 ± 14.2	21.3 ± 22.5	13.11 ± 0.23
J154741+343357	J154741+343350	0.18392	C III	0.5 ± 5.1	67.3 ± 16.6	15.08 ± 0.58
J154741+343357	J154741+343350	0.18392	N III	-15.7 ± 7.1	37.4 ± 20.7	15.27 ± 0.66
J154741+343357	J154741+343350	0.18392	N III	81.0 ± 10.4	11.5 ± 19.8	14.28 ± 0.35
J154741+343357	J154741+343350	0.18392	Si II	-171.7 ± 7.8	5.7 ± 16.8	12.87 ± 0.25
J154741+343357	J154741+343350	0.18392	Si II	-66.1 ± 9.6	11.1 ± 8.3	13.92 ± 0.39
J154741+343357	J154741+343350	0.18392	Si II	-28.1 ± 7.8	13.4 ± 19.3	14.20 ± 0.65
J154741+343357	J154741+343350	0.18392	Si II	14.9 ± 7.8	14.8 ± 7.4	14.00 ± 0.23
J154741+343357	J154741+343350	0.18392	Si III	-9.9 ± 5.1	46.3 ± 13.2	14.31 ± 0.48
J154741+343357	J154741+343350	0.18392	Si III	96.0 ± 4.8	11.6 ± 12.6	13.26 ± 0.53
J154741+343357	J154741+343350	0.18392	Fe III	-83.6 ± 13.4	27.8 ± 26.4	14.05 ± 0.23
J154741+343357	J154741+343350	0.18392	Fe III	-22.8 ± 9.1	17.4 ± 19.5	14.21 ± 0.23
J154741+343357	J154741+343350	0.18392	Fe III	24.1 ± 11.1	14.3 ± 18.8	14.01 ± 0.26
J155504+362847	J155505+362848	0.18926	H I	-60.2 ± 1.0	36.1 ± 2.2	17.60 ± 0.35
J155504+362847	J155505+362848	0.18926	C II	-22.9 ± 5.8	14.3 ± 11.2	14.04 ± 0.22
J155504+362847	J155505+362848	0.18926	C II	-55.5 ± 12.6	82.7 ± 16.0	14.40 ± 0.08
J155504+362847	J155505+362848	0.18926	O VI	-27.5 ± 6.8	35.8 ± 7.4	14.53 ± 0.09
J155504+362847	J155505+362848	0.18926	O VI	-107.9 ± 13.9	41.2 ± 16.6	14.26 ± 0.16
J155504+362847	J155505+362848	0.18926	C III	-69.1 ± 2.5	27.4 ± 2.1	17.15 ± 0.32
J155504+362847	J155505+362848	0.18926	N II	-17.4 ± 9.8	57.5 ± 13.8	14.25 ± 0.08
J155504+362847	J155505+362848	0.18926	N III	-18.9 ± 9.1	22.7 ± 15.7	14.01 ± 0.44
J155504+362847	J155505+362848	0.18926	N III	-78.9 ± 29.7	52.4 ± 30.0	14.24 ± 0.27
J155504+362847	J155505+362848	0.18926	Si II	-23.9 ± 4.0	19.9 ± 6.8	13.11 ± 0.12
J155504+362847	J155505+362848	0.18926	Si II	-99.3 ± 24.7	68.0 ± 36.5	12.94 ± 0.19
J155504+362847	J155505+362848	0.18926	Si III	-43.6 ± 9.6	41.5 ± 8.5	13.57 ± 0.10
J155504+362847	J155505+362848	0.18926	Si III	-114.4 ± 26.7	36.8 ± 24.4	12.89 ± 0.47
J155504+362847	J155505+362848	0.18926	Si IV	-24.7 ± 6.3	23.9 ± 9.5	13.40 ± 0.11
J155504+362847	J155505+362848	0.18926	Si IV	-97.3 ± 8.8	28.4 ± 13.4	13.14 ± 0.18
J160951+353843	J160951+353838	0.28940	H I	-9.5 ± 0.7	57.0 ± 0.8	20.05 ± 0.09
J160951+353843	J160951+353838	0.28940	O I	-90.2 ± 8.6	13.3 ± 14.8	14.68 ± 0.16
J160951+353843	J160951+353838	0.28940	O I	-17.0 ± 1.2	21.8 ± 1.4	16.36 ± 0.04
J160951+353843	J160951+353838	0.28940	O I	110.0 ± 6.0	29.3 ± 3.9	15.49 ± 0.04
J160951+353843	J160951+353838	0.28940	C II	-139.5 ± 7.2	32.2 ± 5.1	14.60 ± 0.09
J160951+353843	J160951+353838	0.28940	C II	-89.7 ± 10.7	10.3 ± 4.6	14.40 ± 0.67
J160951+353843	J160951+353838	0.28940	C II	-10.7 ± 9.5	45.4 ± 5.8	15.43 ± 0.89
J160951+353843	J160951+353838	0.28940	C II	100.9 ± 13.5	27.9 ± 2.2	15.26 ± 0.54
J160951+353843	J160951+353838	0.28940	O VI	-159.5 ± 17.4	32.6 ± 28.9	14.24 ± 0.29
J160951+353843	J160951+353838	0.28940	O VI	-96.5 ± 10.0	26.5 ± 14.1	14.36 ± 0.21
J160951+353843	J160951+353838	0.28940	O VI	-30.0 ± 6.7	18.4 ± 1.7	14.50 ± 0.19
J160951+353843	J160951+353838	0.28940	O VI	8.4 ± 9.1	17.6 ± 16.1	14.29 ± 0.29
J160951+353843	J160951+353838	0.28940	O VI	92.8 ± 5.6	57.8 ± 5.9	15.10 ± 0.04
J160951+353843	J160951+353838	0.28940	C III	-11.6 ± 1.2	73.2 ± 5.7	17.05 ± 0.48
J160951+353843	J160951+353838	0.28940	N II	-152.5 ± 4.4	17.4 ± 6.0	14.15 ± 0.12
J160951+353843	J160951+353838	0.28940	N II	-86.5 ± 22.8	35.3 ± 34.5	14.29 ± 0.42

Table 6 *continued*

Table 6 (*continued*)

Quasar	Galaxy	z_{gal}	ion	v (km s $^{-1}$)	b (km s $^{-1}$)	$\log N$ (log cm $^{-2}$)
J160951+353843	J160951+353838	0.28940	N II	-22.8 ± 5.3	25.5 ± 13.7	14.95 ± 0.21
J160951+353843	J160951+353838	0.28940	N II	40.2 ± 10.0	22.2 ± 17.9	14.13 ± 0.29
J160951+353843	J160951+353838	0.28940	N II	107.4 ± 3.3	27.7 ± 4.6	14.64 ± 0.05
J160951+353843	J160951+353838	0.28940	S III	-8.4 ± 3.0	12.3 ± 5.7	14.71 ± 0.15
J160951+353843	J160951+353838	0.28940	S IV	10.2 ± 4.7	30.7 ± 7.7	14.49 ± 0.07
J225357+160853	J225400+160925	0.390013	H I	-1239.5 ± 3.0	35.9 ± 0.0	14.08 ± 0.06
J225357+160853	J225400+160925	0.390013	H I	-1136.0 ± 3.7	3.9 ± 2.9	13.33 ± 0.43
J225357+160853	J225400+160925	0.390013	H I	-771.7 ± 5.6	11.5 ± 10.8	13.43 ± 0.41
J225357+160853	J225400+160925	0.390013	H I	-711.3 ± 7.8	56.0 ± 9.3	13.97 ± 0.06
J225357+160853	J225400+160925	0.390013	H I	-607.3 ± 8.6	10.7 ± 17.0	12.72 ± 0.28
J225357+160853	J225400+160925	0.390013	H I	68.8 ± 31.5	40.6 ± 18.0	14.42 ± 0.47
J225357+160853	J225400+160925	0.390013	H I	107.6 ± 6.7	22.3 ± 13.7	14.66 ± 0.31
J225357+160853	J225400+160925	0.390013	H I	151.8 ± 5.0	16.9 ± 4.4	14.78 ± 0.11
J225357+160853	J225400+160925	0.390013	H I	216.5 ± 2.8	19.7 ± 3.6	14.03 ± 0.09
J225357+160853	J225400+160925	0.390013	O VI	-1322.5 ± 11.6	6.6 ± 21.4	13.69 ± 0.25
J225357+160853	J225400+160925	0.390013	O VI	-1277.7 ± 5.0	5.5 ± 14.6	13.92 ± 0.72
J225357+160853	J225400+160925	0.390013	O VI	-717.8 ± 2.6	4.2 ± 3.8	14.02 ± 0.42
J225357+160853	J225400+160925	0.390013	O VI	-603.9 ± 7.1	21.7 ± 11.2	13.62 ± 0.14
J225357+160853	J225400+160925	0.390013	O VI	109.6 ± 16.0	21.3 ± 16.4	13.91 ± 0.34
J225357+160853	J225400+160925	0.390013	O VI	149.5 ± 6.5	17.6 ± 7.8	14.24 ± 0.17
J225357+160853	J225400+160925	0.390013	O VI	232.7 ± 14.0	38.0 ± 23.8	13.67 ± 0.19
J225357+160853	J225400+160925	0.390013	C III	77.4 ± 16.0	49.5 ± 15.0	13.85 ± 0.19
J225357+160853	J225400+160925	0.390013	C III	133.7 ± 6.0	21.2 ± 9.2	14.26 ± 0.34
J225357+160853	J225400+160925	0.390013	C III	218.7 ± 6.3	21.5 ± 11.3	13.09 ± 0.13
J225357+160853	J225400+160925	0.390013	N III	241.3 ± 7.8	9.7 ± 13.8	13.61 ± 0.19
J225357+160853	J225400+160925	0.390013	N V	54.4 ± 4.7	8.2 ± 10.8	13.56 ± 0.27
J225357+160853	J225400+160925	0.390013	O III	5.2 ± 14.9	48.3 ± 23.8	14.21 ± 0.15
J225357+160853	J225400+160925	0.390013	O III	101.8 ± 8.4	13.5 ± 17.3	14.01 ± 0.21
J225357+160853	J225400+160925	0.390013	O III	156.6 ± 7.3	16.0 ± 12.8	14.16 ± 0.16
J225357+160853	J225400+160925	0.390013	O III	236.4 ± 8.4	9.6 ± 0.2	13.88 ± 1.42

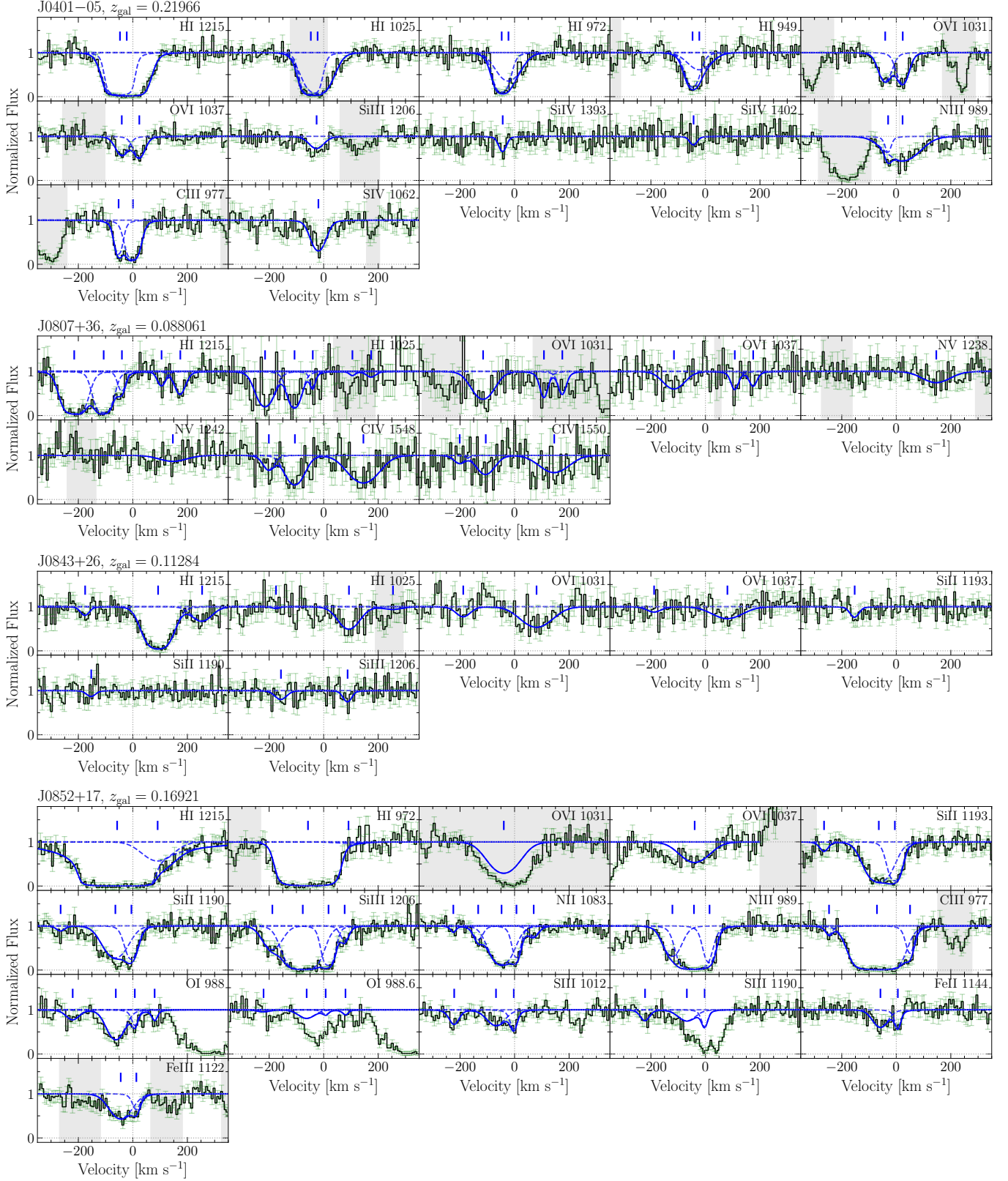
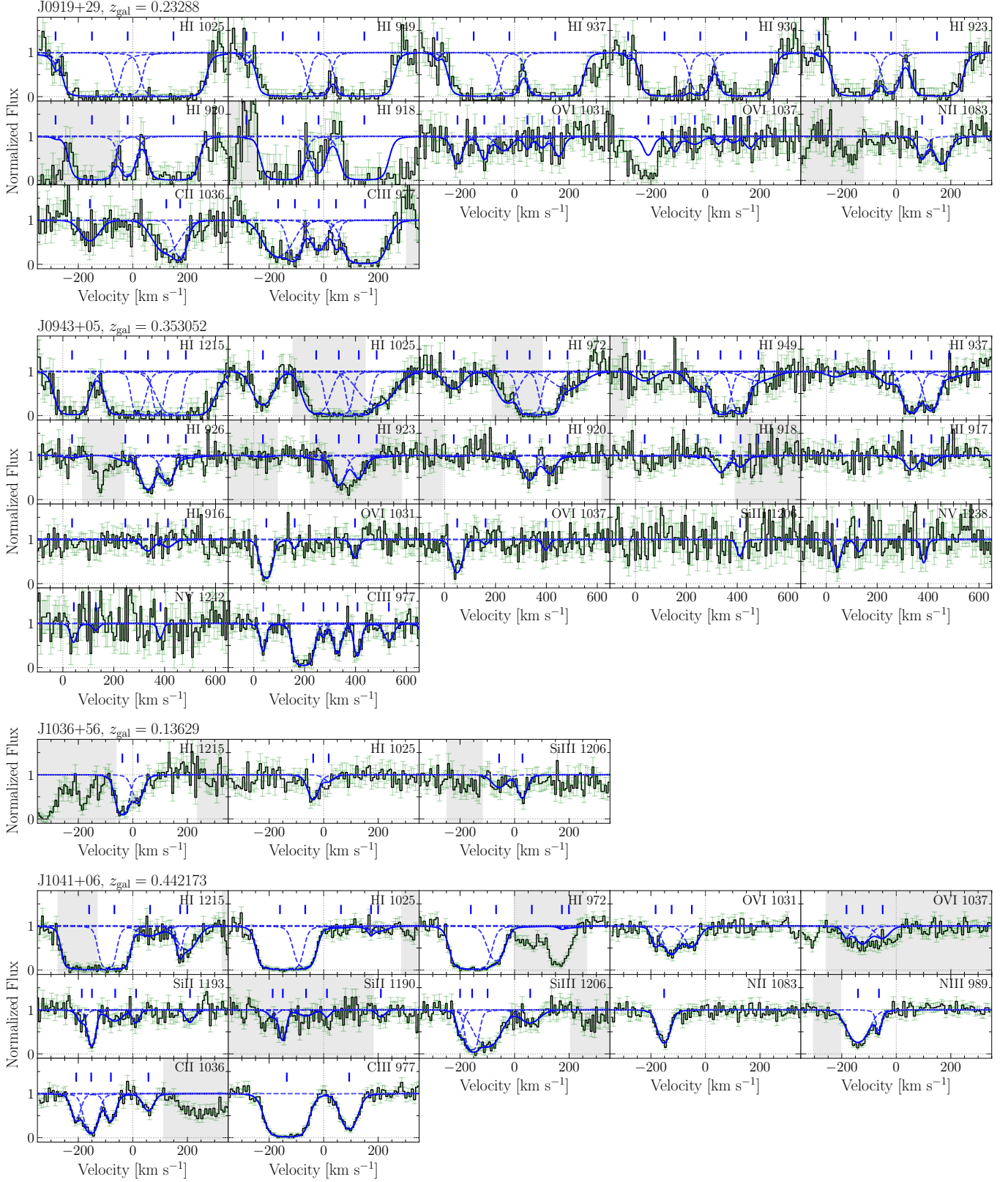
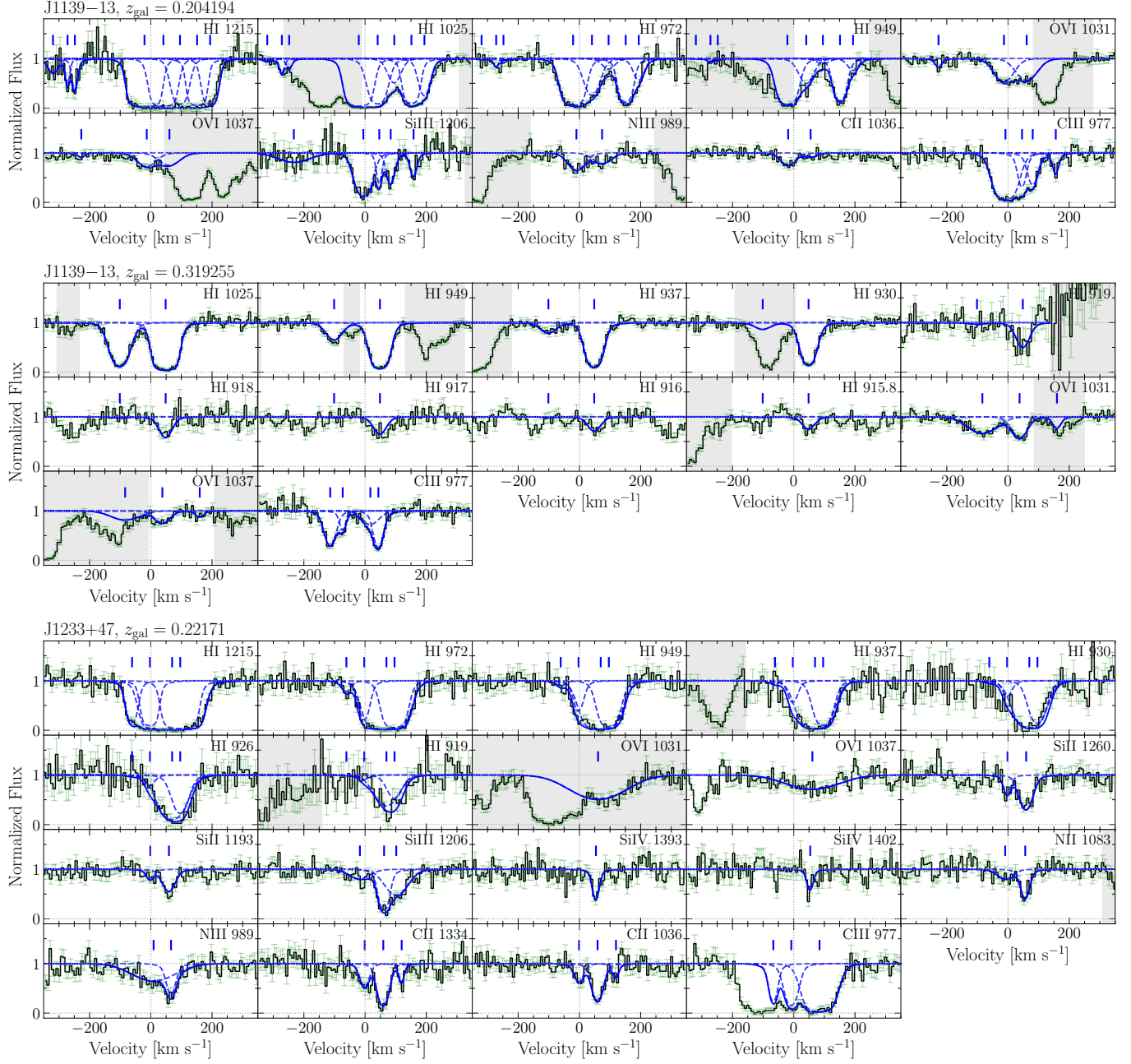


Figure 11. Voigt profile fits of absorption lines relative to the systemic velocity of the host galaxy in individual sightlines. The ionic species are labeled on the upper right. The blue dashed and solid curves show the fitted Voigt profiles for individual velocity components and the overall absorption of the ion, respectively. The blue ticks at the top mark the velocity centroids of individual components. Grey shaded regions are masked during Voigt profile fitting due to contamination from intervening absorbers at other redshifts.

**Figure 11.** (Continued)

**Figure 11.** (Continued)

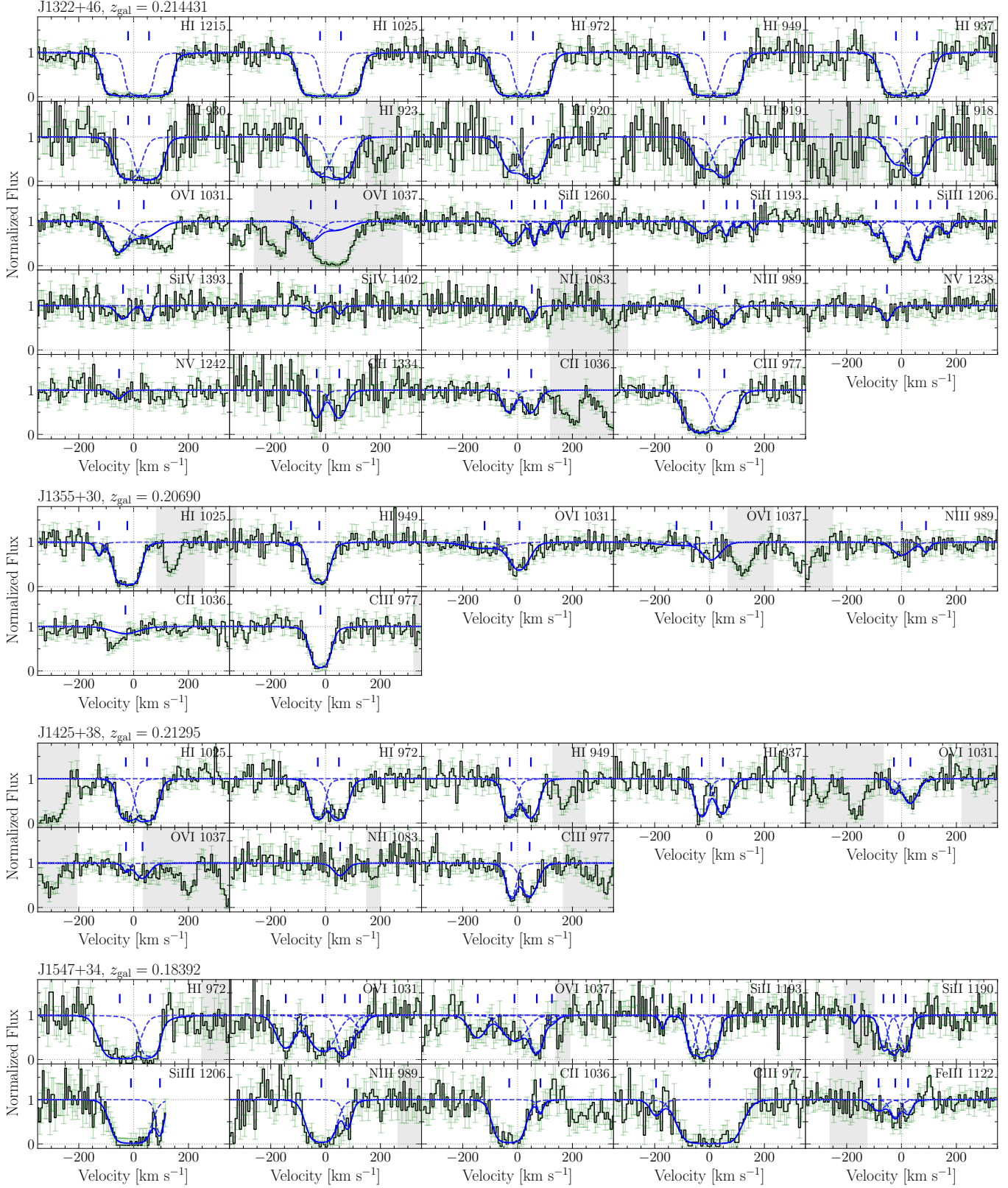
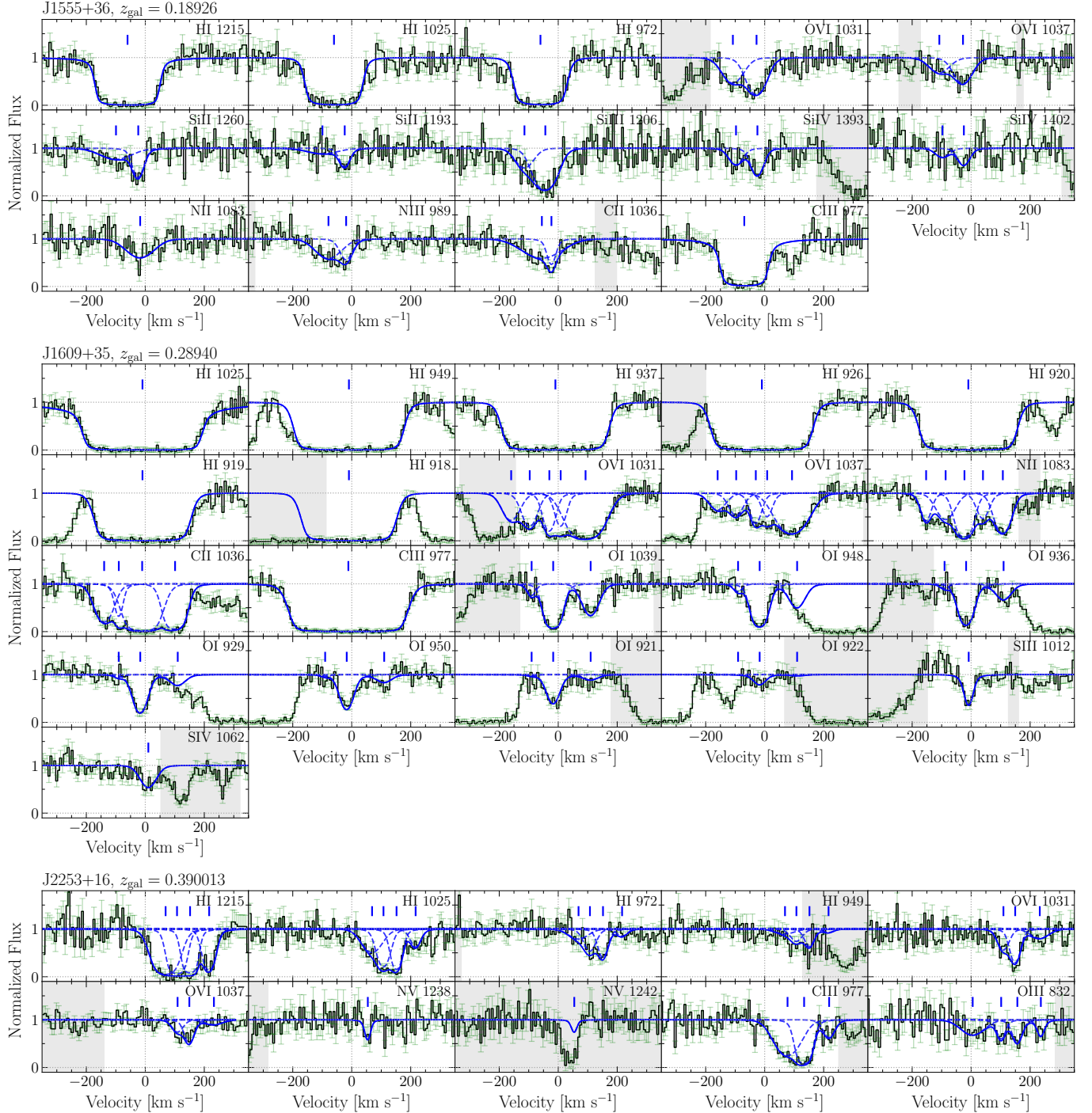


Figure 11. (Continued)

**Figure 11.** (Continued)